J. Fluid Mech. (1994), *vol.* 272, *pp.* 349–381

Effects of convex transverse curvature on wall-bounded turbulence. Part 1. The velocity and vorticity

By JOÃO C. NEVES,[1]† PARVIZ MOIN[1,2] AND ROBERT D. MOSER[2]

[1]Department of Mechanical Engineering, Stanford University, Stanford, CA 94305, USA

[2]NASA Ames Research Center, Moffett Field, CA 94035, USA

(Received 20 November 1992 and in revised form 18 February 1994)

Convex transverse curvature effects in wall-bounded turbulent flows are significant if the boundary-layer thickness is large compared to the radius of curvature (large $\gamma = \delta/a$). The curvature affects the inner part of the flow if a^+, the cylinder radius in wall units, is small.

Two direct numerical simulations of a model problem approximating axial flow boundary layers on long cylinders were performed for $\gamma = 5$ ($a^+ \approx 43$) and $\gamma = 11$ ($a^+ \approx 21$). Statistical and structural data were extracted from the computed flow fields. The effects of the transverse curvature were identified by comparing the present results with those of the plane channel simulation of Kim, Moin & Moser (1987), performed at a similar Reynolds number. As the curvature increases, the skin friction increases, the slope of the logarithmic region decreases and turbulence intensities are reduced. Several turbulence statistics are found to scale with a curvature dependent velocity scale derived from the mean momentum equation. Near the wall, the flow is more anisotropic than in the plane channel with a larger percentage of the turbulent kinetic energy resulting from the streamwise velocity fluctuations. As the curvature increases, regions of strong normal vorticity develop near the wall.

1. Introduction

Turbulent flows that evolve over surfaces with curvature normal to the mean flow are common in engineering applications. However, it is only for strong curvatures that the curvature effects become noticeable. For this reason this flow has received less attention than its planar counterpart, and the body of experimental data available is limited. Transversely curved turbulent flows with large curvature effects occur, for example, over sonar devices towed by long cables. Of particular interest in these flows are the characteristics of the wall pressure fluctuations (Neves & Moin 1994, hereinafter referred to as Part 2).

In order to identify the basic flow unit capable of sustaining turbulence in the plane channel flow, Jimenez & Moin (1991) conducted a series of numerical experiments in which they shortened the length and the width of the computational domain. The resulting flow was called the minimal flow unit and consisted of a single fundamental near-wall structure. Since the transversely curved flow is naturally periodic in the azimuthal direction, and since the near-wall domain becomes smaller as the radius of the cylinder decreases, this flow can be viewed as a natural minimal flow.

† Present address: Naval Research Laboratory, Washington DC 20375-7220, USA.

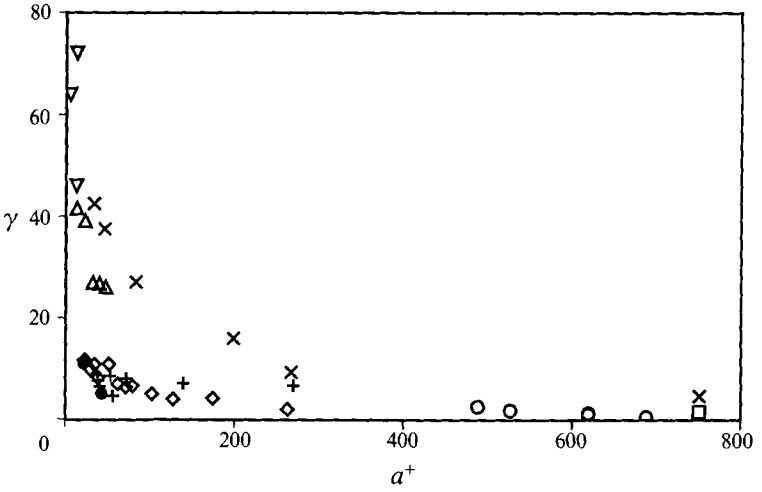

FIGURE 1. Curvature parameters $\gamma = \delta/a$ and a^+ of available experimental data for the axial turbulent flow along a circular cylinder. △, Luxton *et al.* (1984); +, Lueptow *et al.* (1985) and Lueptow & Haritonidis (1987); ×, Willmarth & Yang (1970) and Willmarth *et al.* (1976); ◇, Rao & Keshavan (1972); ○, Afzal & Narasimha (1976); ▽, Richmond (1957); □, Yu (1959); ●, present calculations.

In turbulent flows with transverse curvature there is an additional lengthscale, the cylinder radius, a. The complications introduced by the new lengthscale are evident in the laminar flow. While in the planar case the absence of a lengthscale leads to the self-similar Blasius velocity profile, in the axisymmetric boundary layer there is no self-similar laminar solution (Seban & Bond 1951).

The extra lengthscale gives rise to several flow regimes that are characterized by the ratios of the cylinder radius to the flow lengthscales: the boundary-layer thickness δ, and the viscous lengthscale ν/u_τ. The two resulting parameters, $\gamma = \delta/a$ and $a^+ = au_\tau/\nu$, define a two-dimensional parameter space in which three flow regimes can be identified. If γ is small the curved boundary layer is similar to the planar boundary layer. When the boundary layer is several times thicker than the radius (large γ), the transverse curvature affects the flow differently depending on the magnitude of a^+. If γ is large, and a^+ is also large, then the curvature affects only the outer part of the flow. If γ is large and a^+ is small, the curvature affects both the inner and the outer parts of the flow.

The range of the curvature parameters γ and a^+ that have been investigated experimentally is shown in figure 1. Lueptow (1988) provides a comprehensive review of the experimental investigations of this flow. With the exception of Afzal & Narasimha (1976), whose boundary layers have characteristics very similar to those of the flat plate, γ is large enough in the experiments for the curvature to affect the outer part of the flow. In addition, the experiments of Luxton, Bull & Rajagopalan (1984) ($9 \leqslant a^+ \leqslant 47$ and $26 \leqslant \gamma \leqslant 42$) and of Willmarth *et al.* (1976) ($2 \leqslant \gamma \leqslant 42$ and a^+ as small as 33) are within the range where both the inner and outer parts of the flow should be affected.

One of the characteristics of flows with transverse curvature is a larger skin friction coefficient (C_f) than in a planar flow with similar Reynolds number (see for example Rao & Keshavan (1972) or Willmarth *et al.* (1976)). In the viscous sublayer of transversely curved flows the momentum equilibrium is expressed by $r\tau = a\tau_w$ (Glauert & Lighthill 1955). With the same assumptions as in the planar flow Reid & Wilson (1963) and Rao (1967) proposed a curvature dependent law of the wall,

$U^+ = a^+ \ln(1 + y^+/a^+)$, which predicts curvature effects on the sublayer for sufficiently small a^+.

In order to achieve large γ, experiments are typically performed over long tubes or wires with very small diameter (Luxton *et al.* 1984; Lueptow, Leehey & Stellinger 1985; Lueptow & Haritonidis 1987). In such experimental facilities, the structural isolation of the wires, the aeroelastic interaction between the flow and the wire, the alignment of the cylinder with the mean flow, and the cylinder sag are major concerns. In addition, if a^+ is small, the size of the measuring probe (e.g. hot wire) relative to the cylinder diameter becomes an issue in near-wall measurements. Finally, some of the measurement techniques used are based on the assumption that close to the wall the mean velocity profile is the same as that of the flat plate (e.g. Richmond 1957; Lueptow *et al.* 1985). Attempts to address some of these problems are described by Willmarth & Yang (1970) and Lueptow & Haritonidis (1987).

If γ is not large (Rao & Keshavan 1972; Lueptow *et al.* 1985), the logarithmic region of the mean velocity profile has the same slope as the planar case. This flow regime is described analytically by Afzal & Narasimha (1976) by the method of matched asymptotic expansions. They conclude that when $\gamma = O(1)$ and in the limit of $a^+ \to \infty$, the axisymmetric turbulent boundary layer must have logarithmic and velocity defect profiles of the same form as in the planar turbulent boundary layer. The two parameters in the logarithmic velocity profile are found to depend on γ (Afzal & Narasimha 1976). As γ increases and a^+ decreases, the mean velocity profiles exhibit a logarithmic region with a decreasing slope (Lueptow *et al.* 1985), and for sufficiently large γ and small a^+, the logarithmic region deteriorates and becomes negatively curved (Willmarth *et al.* 1976; Luxton *et al.* 1984). Some effort has been devoted to identifying the curvature dependence of the logarithmic velocity profile, however, it is clear from Lueptow's (1988) review that no consensus exists on this issue. Nevertheless, the available data suggests that when γ is small and a^+ is large the slope of the logarithmic region shows a tendency to scale with γ (Lueptow *et al.* 1985). As γ increases and a^+ decreases, the logarithmic profile depends on both parameters (Willmarth *et al.* 1976; Luxton *et al.* 1984).

The Reynolds shear stress in the outer part of the transversely curved boundary layer is lower than its planar counterpart (Lueptow *et al.* 1985). Reynolds shear stress quadrant detection in the transversely curved turbulent boundary layers are similar to those in the planar geometry (Lueptow & Haritonidis 1987). At $y^+ \approx 39$, Lueptow & Haritonidis (1987) measure fractional contributions from second and fourth quadrant events higher than in the planar case for weak events. Intense events are found to have a lower contribution to the Reynolds shear stress.

The axial and normal turbulence intensities measured by Luxton *et al.* (1984) or Lueptow & Haritonidis (1987) are also lower than their flat plate counterparts in the outer part of the boundary layer. Close to the wall ($y^+ < 20$), the measured axial intensities have magnitudes similar to those of the planar case, with maxima ($(\overline{v_z^2})^{1/2}/u_\tau \approx 3.2$) also located at $y^+ \simeq 12$.

Through a visualization study of axial flow over a cylinder, Lueptow & Haritonidis (1987) observed large-scale structures moving across the cylinder. Since these large structures have an azimuthal (spanwise) velocity component, it is expected that they should significantly affect the azimuthal velocity intensity fluctuations, which unfortunately were not measured. Similar large-scale structures were also observed by Luxton *et al.* (1984), but only for larger curvatures ($\gamma \geqslant 20$). Luxton *et al.* (1984) suggested that these large-scale structures are important for turbulence generation in this flow.

The current study was undertaken to address several issues that have not yet been addressed in the literature on transversely curved boundary layers. In particular, many statistical quantities of importance to both modelling and theory are not available (e.g. full Reynolds stress tensor, terms in the balance equations for the Reynolds stress and vorticity statistics), and thus the impact of transverse curvature on these quantities is not known. Also, little is known about the effects of transverse curvature on the familiar near-wall turbulent structures. Finally, because of its relevance to sonar applications, the behaviour of the wall pressure is of particular interest in this flow. In this paper, the statistical characteristics and instantaneous structure of the velocity field are presented. The wall pressure is discussed in Part 2.

A brief description of the model problem and numerical techniques is given in §2. In §3 the properties of the mean flow are discussed and compared with the available experimental data. In §4 turbulence intensities and the Reynolds shear stress are presented and a curvature dependent local velocity scale is derived from the momentum equations. Vorticity statistics are presented in §5. Finally, the instantaneous structural characteristics of the flow are presented via contour plots of instantaneous fields in §6.

2. The model flow and numerical methods

A spatially developing boundary layer on a long cylinder, which is the physical flow of interest, has two features that complicate numerical simulation; the spatial growth and the semi-infinite domain. To avoid these difficulties we consider a model problem that has the key features of a transversely curved boundary layer (i.e. a wall-bounded shear flow with transverse curvature of radius much smaller than the shear-layer thickness) but which does not have these complicating features. The model is the axial flow between concentric cylinders driven by a mild streamwise pressure gradient. The width of the gap between the cylinders (δ) corresponds roughly to the thickness of a boundary layer, and we define the curvature parameter $\gamma = \delta/a$, where a is the inner cylinder radius. Unless otherwise stated, δ is used along with the friction velocity u_τ for non-dimensionalization throughout the remainder of the paper, and the density is assumed to be one. Thus, in these units the radial (r) domain is $r \in [a', a'+1]$, and the curvature parameter is $\gamma = 1/a'$, where $a' = a/\delta$ is the non-dimensional cylinder radius. The non-dimensional radial distance from the cylinder is $y = r - a'$. In what follows, the prime will be dropped for simplicity (thus a now refers to the non-dimensional radius). The mild streamwise pressure gradient that drives the flow is determined by requiring that the total mass flux be constant, and like the plane channel, this flow becomes statistically stationary. In addition to γ, the model flows can be characterized by one of several Reynolds numbers. The four that are reported here are $Re_\tau = u_\tau \delta/\nu$, $Re_\delta = U_\infty \delta/\nu$, where U_∞ is the mean velocity at the outer cylinder (see below), $Re_a = U_\infty a\nu$ and $a^+ = u_\tau a/\nu$.

At the inner cylinder ($r = a$), the velocity (V is the total velocity, v is the fluctuating velocity) satisfies no-slip boundary conditions,

$$V|_{r=a} = 0. \tag{1}$$

To better approximate the properties of a boundary layer, the surface shear stress is made zero at the outer cylinder, thus

$$V_r|_{r=a+1} = 0, \quad \frac{\partial}{\partial r}\left(\frac{V_\theta}{r}\right)\bigg|_{r=a+1} = 0, \quad \frac{\partial V_z}{\partial r}\bigg|_{r=a+1} = 0. \tag{2}$$

γ	5	11
L_z	4π	6π
L_z^+	2676	4656
$L_{\theta_i}^+ = 2\pi a^+$	268	141
$L_{\theta_0}^+ = 2\pi(a^+ + \delta^+)$	1608	1692
$\Delta_z^+ = L_z^+/N_z$	14	14
$\Delta_{\theta_i}^+ = L_{\theta_i}^+/N_\theta$	4	1
$\Delta_{\theta_0}^+ = L_{\theta_0}^+/N_\theta$	25	13
(N_z, N_r, N_θ)	(192, 96, 65)	(320, 96, 129)

TABLE 1. Grid resolution parameters

This model problem probably does not provide an accurate representation of the outer regions of a boundary layer owing to the truncated domain. For example, the large-scale viscous–inviscid interactions of the type reported by Luxton *et al.* (1984) and Lueptow & Haritonidis (1987) are precluded. However, it is expected that the near-wall features of the flow will be insensitive to the details of the outer boundary conditions. This is supported by our experience in comparing the plane channel flow of Kim, Moin & Moser (1987) with the turbulent boundary layers of Spalart (1988). Furthermore, the effects of the outer boundary on the flow near the wall diminishes with increasing curvature (see the vorticity contours in figure 27).

In the azimuthal (θ) direction, the flow is naturally periodic. In the streamwise or axial direction (z), periodic boundary conditions with period L_z are used. The variation of the velocities in these directions are represented by Fourier expansions. In the radial direction, Chebyshev polynomial expansions (see e.g. Gottlieb & Orszag 1977) are used. These expansions promote high resolution at the boundaries of the domain ($r = a$ and $r = a+1$). This is appropriate for the inner boundary where no-slip conditions are imposed. However, at the outer edge of the domain, fine resolution is not necessary because no sizeable velocity gradients are expected there. To avoid this waste of resolution, the radial coordinate mapping

$$r = a - \tfrac{1}{2}(1-\beta)\left(\frac{1+\xi}{\beta-\xi}\right), \tag{3}$$

is used, which increases the resolution close to the cylinder surface at the expense of the resolution at the outer edge of the computational domain. In this expression, the Chebyshev variable $\xi \in [-1, 1] \Leftrightarrow r \in [a, a+1]$ and the parameter $\beta = 6$ was used.

The spatial resolution parameters describing the two turbulent flow simulations reported here are shown in table 1. Note that the effective azimuthal resolution, $\Delta\theta = 2\pi r/N_\theta$, is the coarsest at the outer edge of the domain ($r = a+1$). On the other hand, near the wall the simulations are very well resolved in the azimuthal direction. At the outer edge, the azimuthal resolution appears to be adequate as shown by the velocity spectra. Likewise, the axial resolution appears to be adequate (Neves, Moin & Moser 1992). The length of the computational domain in the axial direction is set to be sufficiently large to ensure that the velocity is decorrelated for separations larger than half of the computational box, so that the imposed periodic boundary conditions will have minimal effects on the turbulence.

In cylindrical coordinates the Navier–Stokes equations are coupled through the advection terms as well as through the viscous terms. In the numerical approach adopted, the curvature terms of the viscous operators are treated explicitly (Neves

et al. 1992) without imposing a severe stability limitation. The pressure is calculated through a variant of the method of Kleiser & Schumann (1981) and continuity at the boundaries is imposed accordingly (see Neves *et al.* (1992) for details). In addition, a dependent variable $\Upsilon = \partial V_\theta/\partial z - \partial V_z/\partial\theta$ is defined. The velocity field is obtained from the solution of the partial differential equations for V_r and Υ and an algebraic system of equations for the Fourier coefficients of V_θ and V_z. A semi-implicit second-order accurate time-advancement scheme was used. The numerical method was validated by calculating several two- and three-dimensional states of the Taylor–Couette flow. The results of these tests were in very good agreement with both experiments and previous calculations (Donnelly & Simon 1960; Moser & Moin 1984; King *et al.* 1984), indicating that the numerical method provides an accurate representation of the Navier–Stokes equations in this geometry.

To begin the simulations, a mean velocity profile with the desired mass flux is specified along with random velocity fluctuations. The mass flux and viscosity are selected to obtain the desired friction velocity Reynolds number (approximately). For each flow the equations were integrated until the solution became statistically stationary, so the only important property of the initial conditions is the mass flux. After becoming stationary, the simulations were continued to accumulate statistics.

3. Mean velocity statistics

Mean flow parameters for the present transversely curved flow simulations as well as for the plane channel ($\gamma = 0$) are reported in table 2. Because the Reynolds numbers of the three simulations are similar, the differences in table 2 are due to the transverse curvature. For comparison, tables 3, 4 and 5 contain the mean flow parameters of the experiments of Willmarth *et al.* (1976), Luxton *et al.* (1984) and Lueptow & Haritonidis (1987), respectively. In agreement with experimental observations, the skin friction coefficient,

$$C_f = 2\left(\frac{u_\tau}{U_\infty}\right)^2, \tag{4}$$

increases with increasing curvature (by as much as 63% for $\gamma = 11$) when compared with a plane channel flow with comparable Reynolds number. However, in the simulations the magnitude of this increase is larger than has been observed experimentally (see below). In table 2 the boundary-layer displacement and momentum thicknesses (δ^* and θ^* respectively) were computed using the following expressions given by Luxton *et al.* (1984)

$$(a+\delta^*)^2 - a^2 = 2\int_a^{a+1}\left(1-\frac{\bar{V}_z}{U_\infty}\right) r\,\mathrm{d}r, \tag{5}$$

$$(a+\theta^*)^2 - a^2 = 2\int_a^{a+1}\left(\frac{\bar{V}_z}{U_\infty}\right)\left(1-\frac{\bar{V}_z}{U_\infty}\right) r\,\mathrm{d}r. \tag{6}$$

The expression for the displacement thickness (equation (5)) is consistent with the usual mass flux displacement argument, and the momentum thickness defined by (6) arises in the axisymmetric integral momentum equation. In this sense, the two definitions have the same physical meaning as their planar counterparts, and in the flat plate limit ($\gamma \to 0$), (5) and (6) reduce to their planar counterparts. Luxton *et al.* (1984) measured δ^* and θ^* according to the above expressions and found values higher than in the simulations. This is probably a result of the larger γ in the experiments. The

γ	0	5	11
a^+	—	43	21
C_f	6.04×10^{-3}	8.07×10^{-3}	9.87×10^{-3}
Re_δ	3300	3368	3418
Re_τ	180	214	239
Re_a	—	674	311
δ^*	0.141	0.154	0.152
θ^*	0.087	0.123	0.131
H	1.62	1.25	1.15

TABLE 2. Mean flow parameters

γ	4.7	16	37.5
a^+	751	198	46
C_f	3.04×10^{-3}	4.18×10^{-3}	7.84×10^{-3}
Re_δ	90380	69280	27600
Re_a	19230	4330	736

TABLE 3. Experimental mean flow parameters (Willmarth *et al.* 1976)

γ	26	26.9	41.6
a^+	47.4	32.1	13
C_f	7.3×10^{-3}	0.01	0.017
Re_δ	20386	12252	5962
Re_a	785	455	140
δ^*	0.184	0.185	0.187
θ^*	0.181	0.182	0.182
H	1.014	1.02	1.03

TABLE 4. Experimental mean flow parameters (Luxton *et al.* 1984)

γ	6.74	7.16	8.0
a^+	288	144	72
C_f	3.5×10^{-3}	3.8×10^{-3}	4.1×10^{-3}
Re_δ	46330	23700	12800
Re_a	6419	3209	1605

TABLE 5. Experimental mean flow parameters (Lueptow & Haritonidis 1987)

shape factors ($H = \delta^*/\theta^*$) measured by Luxton *et al.* (1984) are around unity, whereas the shape factor in the simulations is larger than one and decreases with increasing γ owing to an increase in the momentum thickness.

3.1. *The mean velocity profile*

The mean velocity profiles of the two transversely curved flows ($\gamma = 5$ and 11) are compared to that in the plane channel flow in figure 2. Because of the small values of a^+, the viscous sublayer mean velocity profiles are slightly affected by the curvature of the wall. In contrast, most experiments (Rao & Keshavan 1972; Willmarth *et al.* 1976;

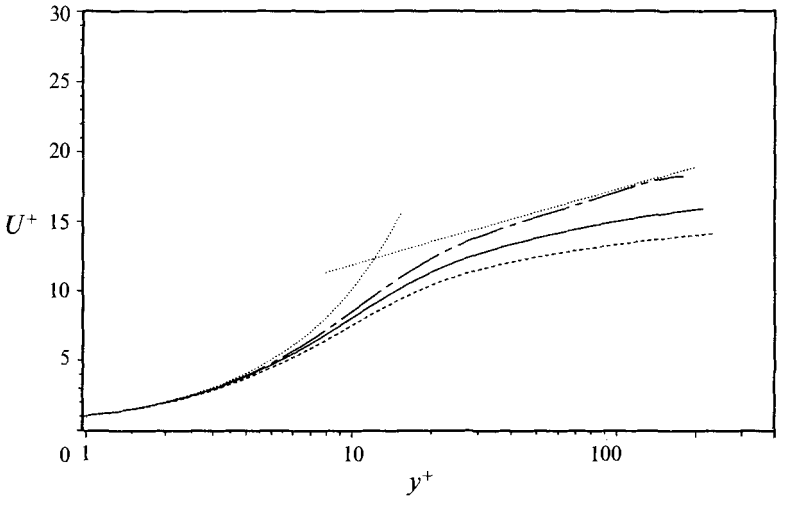

FIGURE 2. Mean-velocity profiles: ———, plane channel (Kim *et al.* 1987); cylinders with ——, $\gamma = 5$ and – – –, $\gamma = 11$; ·····, planar law of the wall, $U^+ = y^+$, and log law, $U^+ = 2.5\ln(y^+) + 5.5$.

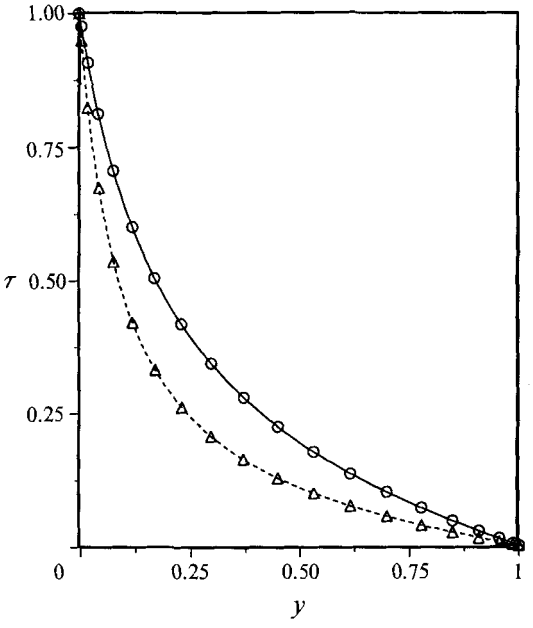

FIGURE 3. Total stress: analytical for cylinders with ——, $\gamma = 5$ and – – –, $\gamma = 11$; computed results with ○, $\gamma = 5$ and △, $\gamma = 11$.

Lueptow *et al.* 1985) find no effect of curvature in the mean velocity profile for $y^+ < 20$. Clearly, in many of these experiments a^+ is too large for there to be a perceptible inner-layer effect (for example $a^+ \approx 140$ and $\gamma \approx 7$ in Lueptow & Haritonidis 1987). However, even in experiments in which the values of a^+ are close to or below those of the simulations (e.g. Luxton *et al.* 1984; Willmarth *et al.* 1976), the measured mean velocity profiles appear to agree with the planar mean velocity profile for $y^+ < 20$. This discrepancy may be caused by the difficulties in estimating the friction velocity in the

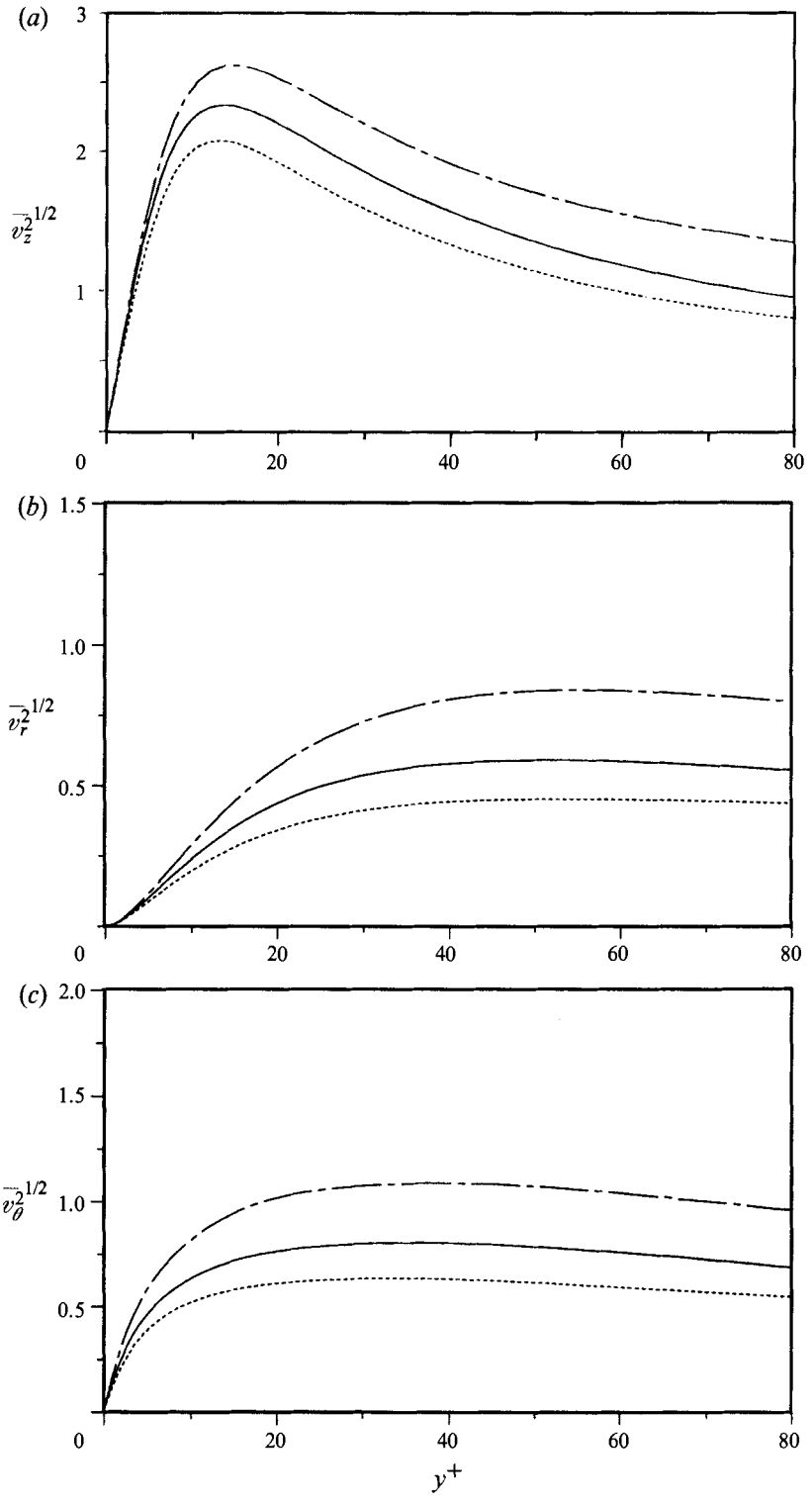

FIGURE 4. Root-mean-square velocity fluctuations: (*a*) axial velocity, (*b*) normal velocity, (*c*) azimuthal velocity; ———, plane channel (Kim *et al.* 1987); cylinders with ——, $\gamma = 5$ and – – –, $\gamma = 11$.

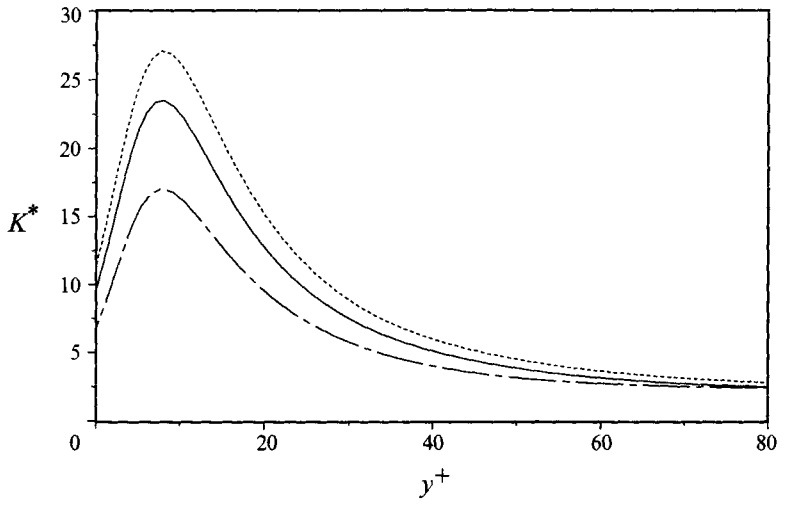

FIGURE 5. The energy partition parameter $K^* = 2\overline{v_z^2}/(\overline{v_r^2}+\overline{v_\theta^2})$: ———, plane channel (Lee *et al.* 1990); cylinders with ——, $\gamma = 5$ and – – –, $\gamma = 11$.

experiments. For example, in Willmarth *et al.* (1976) and Lueptow *et al.* (1985), the friction velocity is estimated by fitting the near wall data to the flat-plate law of the wall. This can only be valid when a^+ is large enough for the mean velocity profile to be unaffected in the fitting region. The range in y^+ over which the data was fitted is not specified in these papers. However, the skin friction is under estimated by 13% and 8% when a similar procedure is applied to the simulation data ($a^+ = 21$ and 43, respectively) by matching the flat plate law of the wall at $y^+ = 12$.

In the planar boundary layer, the assumption that in the viscous sublayer the total stress is dominated by the viscous stress leads to the near-wall velocity profile, $U^+ = y^+$. For the axisymmetric boundary layer in the absence of a pressure gradient, the mean momentum equilibrium in the viscous sublayer is expressed by $\tau/\tau_w = a/r$ (Glauert & Lighthill 1955). Assuming that the Reynolds shear stress is negligible in comparison to the viscous stress leads to the analogous profile for axisymmetric flows (Reid & Wilson 1963; Rao 1967),

$$U^+ = a^+ \ln\left(1+\frac{y^+}{a^+}\right). \tag{7}$$

Note that, to second order in y^+, (7) is given by

$$U^+ = y^+\left(1+\frac{y^+}{2a^+}\right). \tag{8}$$

Thus, the mean velocity in the viscous sublayer of transversely curved flows is equal to that of the planar viscous sublayer ($U^+ = y^+$) plus a curvature dependent correction. Clearly, if a^+ is large the mean velocity profile near the wall does not deviate appreciably from the planar case. The mean velocity profiles given by (7) are better approximations to the computed near-wall velocity profiles than the planar law of the wall.

As observed in several experiments (Lueptow *et al.* 1985; Luxton *et al.* 1984; Willmarth *et al.* 1976), the slope of the mean velocity profile in the logarithmic region decreases with increasing curvature and the profiles become negatively curved.

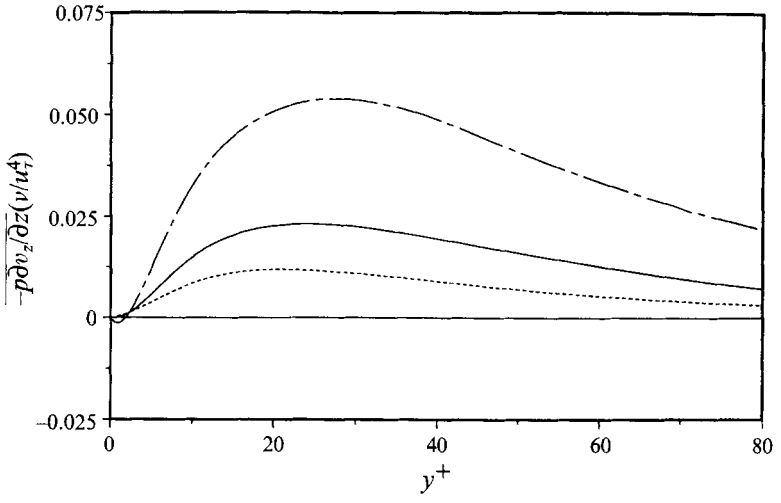

FIGURE 6. Pressure–strain term from the budget equation for $\overline{v_z^2}$ normalized by ν and u_τ: cylinders with ——, $\gamma = 5$ and – – –, $\gamma = 11$; – – – –, plane channel (Mansour *et al.* 1988).

However, the dependence of the slope of the logarithmic region on the curvature is larger in the simulations than in experiments (Willmarth *et al.* 1976). Lueptow *et al.* (1985), for example, show that the slope of the logarithmic region is universal for small γ. This is not surprising because for small γ the curvature effects are limited to the outer part of the boundary layer in high-Reynolds-number flows. Based on the same measurements, Lueptow *et al.* (1985) also argued that the slope of the logarithmic region is not a function of a^+. The latter conclusion, however, is questionable because in those experiments a^+ is consistently large. These observations are in general agreement with the asymptotic analysis of the axisymmetric momentum equations in the limit of $\gamma = O(1)$ and $a^+ \to \infty$ (Afzal & Narasimha 1976). To lowest order in this limit, the axisymmetric boundary layer has both a logarithmic region and an outer velocity defect law. For smaller a^+ the parameters of the velocity profile in the two regions depend on both γ and a^+. The measurements of Luxton *et al.* (1984) for flows with larger γ than in the present simulations but with similar a^+ show logarithmic region slopes comparable to those reported here. The lack of consensus on this issue is summarized in the review of Lueptow (1988). A parametric study is necessary before a conclusion can be reached, but it seems that the slope of the logarithmic region is a function of both a^+ and γ when both the inner and outer layers are affected.

4. Turbulence statistics

The statistical steady state is characterized by the equilibrium between the mean total stress and the applied streamwise pressure gradient. For the flows under consideration this is expressed by

$$-\overline{uv} + \frac{1}{Re}\frac{\mathrm{d}\bar{V}_z}{\mathrm{d}r} = \frac{a}{r}\frac{(a+1)^2 - r^2}{(a+1)^2 - a^2}. \tag{9}$$

Figure 3 shows the total stress (computed and analytic) for the present simulations. The computed and analytic curves coincide in both simulations, indicating that the statistical steady state has been achieved.

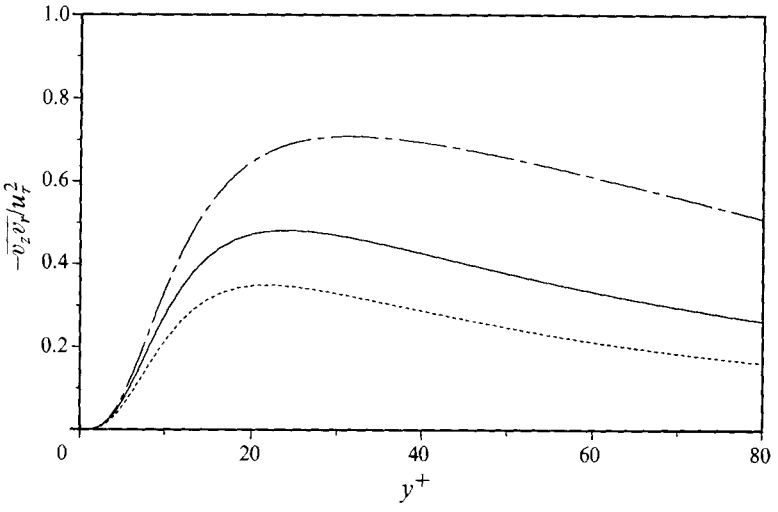

FIGURE 7. Reynolds shear stress normalized by u_τ: cylinders with ——, $\gamma = 5$ and – – –, $\gamma = 11$; ———, plane channel (Kim *et al.* 1987).

4.1. *The turbulence intensities*

Turbulence intensities normalized with the friction velocity decrease throughout the layer as the curvature increases (figure 4). The streamwise component is the most energetic and the location of its maximum moves slightly towards the wall as the curvature increases. The smaller turbulent kinetic energy in the transversely curved flows can be attributed in part to the smaller surface area over which vorticity fluctuations can be generated relative to the volume of turbulent flow supported. The cylinder surface is apparently not less efficient as a source of turbulent kinetic energy; rather it has to supply a larger volume. Experimental data also show a reduction in the turbulence intensities with increasing curvature (Lueptow *et al.* 1985; Lueptow & Haritonidis 1987; Luxton *et al.* 1984). For experiments with comparable a^+, Luxton *et al.* (1984) report a maximum value of the streamwise intensity, $(\overline{v_z^2})^{1/2}/U_\infty \approx 0.16$, similar to the simulation result of 0.15. However, for the larger a^+ experiments of Lueptow & Haritonidis (1987), the maximum value of $(\overline{v_z^2})^{1/2}/u_\tau$ of 3.3 is higher than in the flat plate and is contrary to the simulation results.

Similarly, the normal ($(\overline{v_r^2})^{1/2}$) and azimuthal ($(\overline{v_\theta^2})^{1/2}$) intensities are lower than in the planar case. However, the reductions in the normal and azimuthal intensities are greater than that of the axial (streamwise) intensity. The energy partition parameter (Lee, Kim & Moin 1990),

$$K^* = \frac{2\overline{v_z^2}}{\overline{v_r^2}+\overline{v_\theta^2}}, \tag{10}$$

shown in figure 5, is a measure of the relative contribution to the turbulent kinetic energy of the streamwise turbulence intensity and the intensities normal to the mean flow. The attenuation of the normal and azimuthal velocity fluctuations is strongest for $y^+ < 30$ and increases with curvature.

Figure 5 suggests that the transfer of energy from the streamwise velocity component to the other two velocity components is reduced as the curvature increases. In the budget equations of the turbulence intensities the pressure–strain terms are responsible for the intercomponent energy transfer. As shown in figure 6, as the curvature increases the pressure–strain term in the budget of the axial (streamwise) intensity decreases significantly throughout the layer.

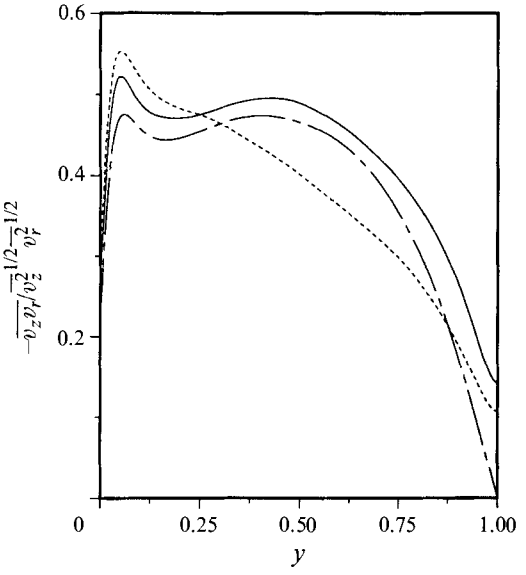

FIGURE 8. Correlation coefficient: cylinders with ——, $\gamma = 5$ and – – –, $\gamma = 11$; – – – –, plane channel (Kim *et al.* 1987).

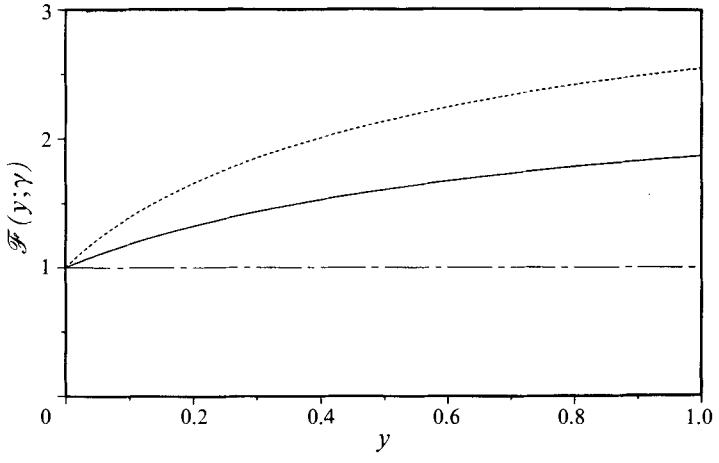

FIGURE 9. Velocity scaling function $\mathscr{F}(y;\gamma)$: – – – –, plane channel ($\gamma = 0$); cylinders with ——, $\gamma = 5$ and – – –, $\gamma = 11$.

4.2. *The Reynolds shear stress*

The Reynolds shear stress (figure 7) is also reduced by curvature. The location of the maximum of the Reynolds shear stress profile is a function of γ and moves towards the wall with increasing curvature. However, this does not affect the position of the maximum in the production ($-\overline{v_z v_r}\,\mathrm{d}\bar{V}_z/\mathrm{d}y$) of turbulent kinetic energy ($y^+ \simeq 12$, see figure 11*b*). In the outer layer the measurements of Lueptow *et al.* (1985) show that the Reynolds shear stress decreases with increasing curvature in agreement with the simulation results. In the inner layer, the measurements of the Reynolds shear stress reported by Lueptow *et al.* (1985) for the transversely curved flows do not differ appreciably from those of the planar case.

The velocity correlation coefficient, shown in figure 8, suggests that there are

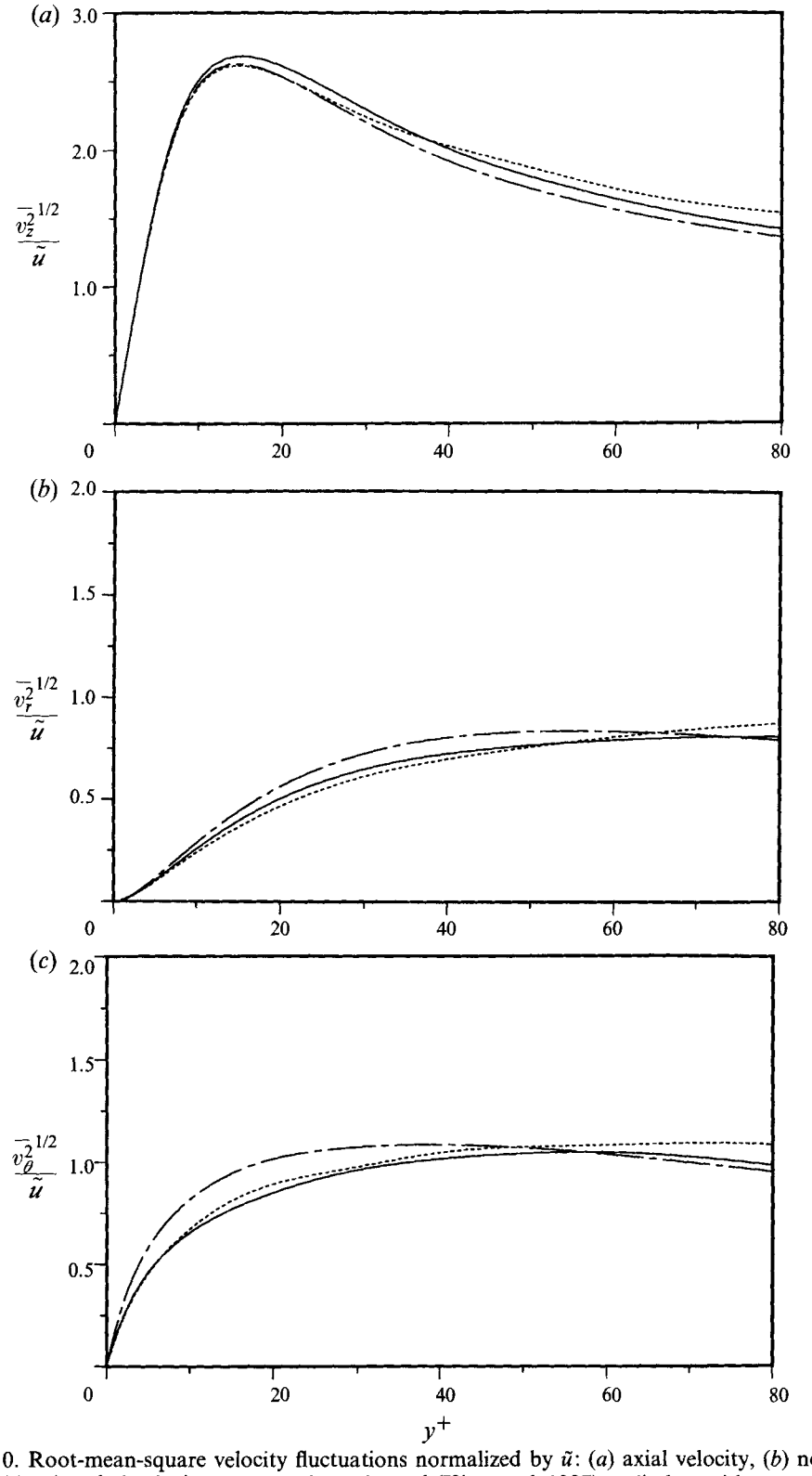

FIGURE 10. Root-mean-square velocity fluctuations normalized by $\tilde{u}$: (*a*) axial velocity, (*b*) normal velocity, (*c*) azimuthal velocity; ———, plane channel (Kim *et al.* 1987); cylinders with ——, $\gamma = 5$ and – – –, $\gamma = 11$.

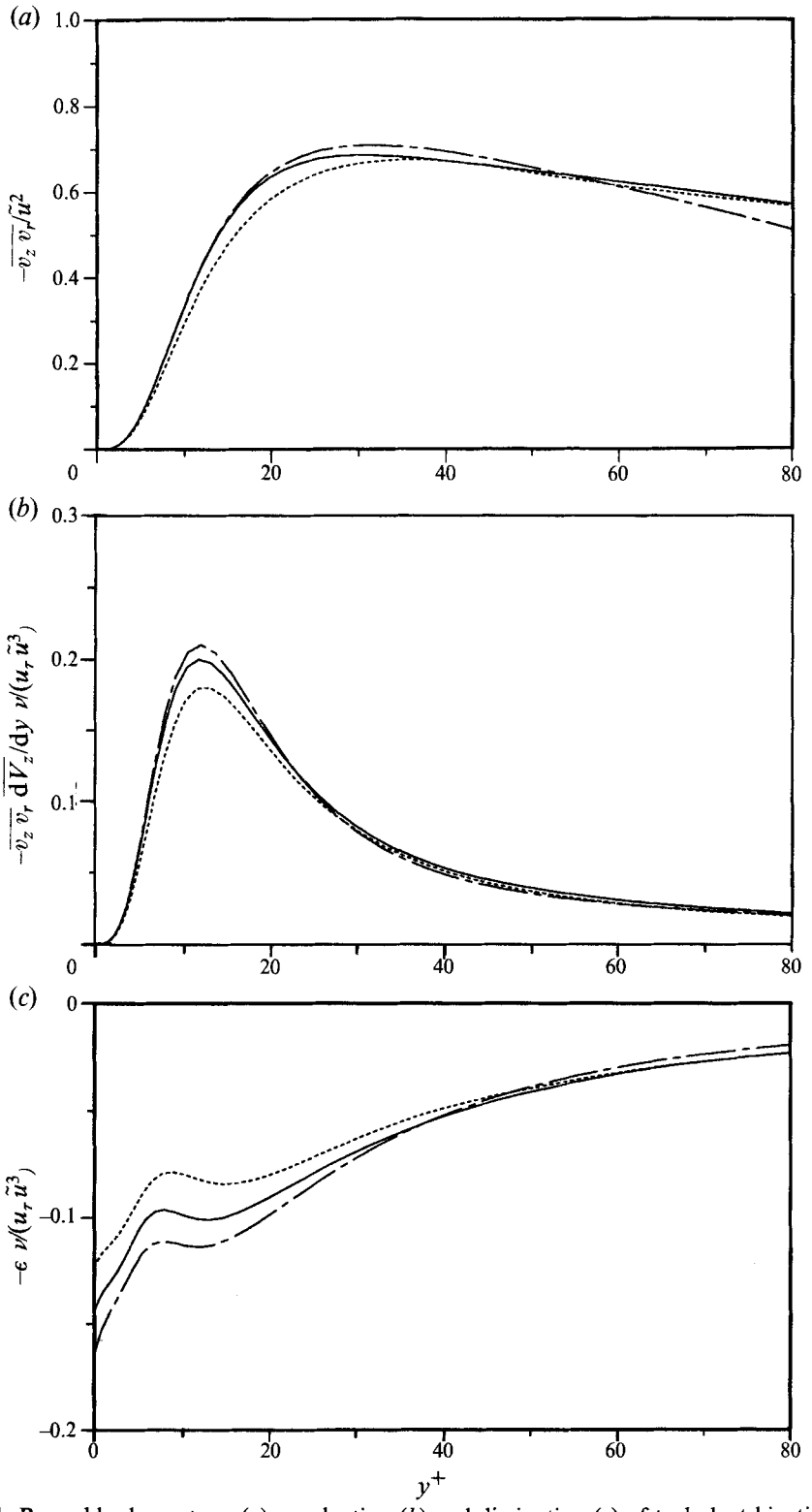

FIGURE 11. Reynolds shear stress (*a*), production (*b*) and dissipation (*c*) of turbulent kinetic energy normalized by ν/u_τ and $\tilde{u}$: cylinders with ——, $\gamma = 5$ and – – –, $\gamma = 11$; — — —, plane channel (Mansour *et al.* 1988).

important differences both between the two transversely curved flows as well as between them and the plane channel. Close to the wall ($y < 0.2$), the streamwise and wall normal velocity fluctuations are increasingly better correlated as curvature increases. Away from the wall, the large curvature case ($\gamma = 11$) shows a significant reduction in the correlation coefficient. This may be an indication of flow stabilization, although for $\gamma = 11$ the flow is a self sustaining turbulent flow and reaches statistically steady state (figure 3).

4.3. *The velocity scaling*

As a function of the distance to the wall the total stress, equation (9) can be rewritten as

$$\tau = u_\tau^2 \frac{1}{1+\gamma y}\left(1+\frac{\gamma y}{\gamma+2}\right)(1-y). \tag{11}$$

In this form it can be easily compared with its planar counterpart $\tau = u_\tau^2(1-y)$, which is a linear function of y. These two expressions suggest the definition of a new y-dependent velocity scale for the transversely curved flows

$$\tilde{u} = u_\tau / \mathscr{F}(y;\gamma), \tag{12}$$

where

$$\mathscr{F}(y;\gamma) = \left((1+\gamma y)\left(1+\frac{\gamma y}{\gamma+2}\right)^{-1}\right)^{1/2}. \tag{13}$$

This function is plotted in figure 9. In the planar limit ($\gamma \to 0$), $\mathscr{F}(y;\gamma) \to 1$ and the planar velocity scale, $\tilde{u} = u_\tau$, is recovered.

When scaled with $\tilde{u}$, the turbulence intensities and Reynolds shear stress profiles of the two curved flows collapse (figures 10 and 11*a*). The collapse with the plane channel stresses is also satisfactory except for the azimuthal (spanwise) turbulence intensity. The turbulence production and viscous dissipation scale with $\tilde{u}$ in the outer part of the layer but apparently not near the wall, as shown in figures 11(*b*) and 11(*c*), respectively.

4.4. *Higher-order statistics*

The correlation coefficient profiles (figure 8) suggest that the Reynolds-shear-stress-producing events are strongly affected by curvature. The contribution of flow events to the production (or consumption) of turbulent kinetic energy can be assessed through the quadrant analysis of the Reynolds shear stress (Willmarth & Lu 1972). Two types of fluid motions contribute to positive $v_z v_r$, the outward motion of high-speed fluid ($v_z > 0$ and $v_r > 0$) and the inward motion of low-speed fluid ($v_z < 0$ and $v_r < 0$). On the other hand, the inward motion of high-speed fluid ($v_z > 0$ and $v_r < 0$) and the outward motion of low-speed fluid ($v_z < 0$ and $v_r > 0$) contribute to negative Reynolds shear stress and production of turbulent kinetic energy. In transversely curved turbulent flows, the partition of the Reynolds shear stress among the four quadrants is very similar to that of the plane channel, as shown in figure 12. It is a characteristic of wall-bounded flows that the Reynolds shear stress is dominated by the second-quadrant events ($v_z < 0$ and $v_r > 0$) in the outer layer, and by the fourth-quadrant events ($v_z > 0$ and $v_r < 0$) in the inner layer. The crossover point between the dominance of second- and fourth-quadrant events occurs at the same distance from the wall ($y^+ \simeq 12$) as in the plane channel.

Likewise, at a given distance from the wall, the fractional contributions to the Reynolds shear stress in the transversely curved flows are similar to the corresponding contributions in the plane channel (Neves *et al.* 1992). This invariance of the fractional

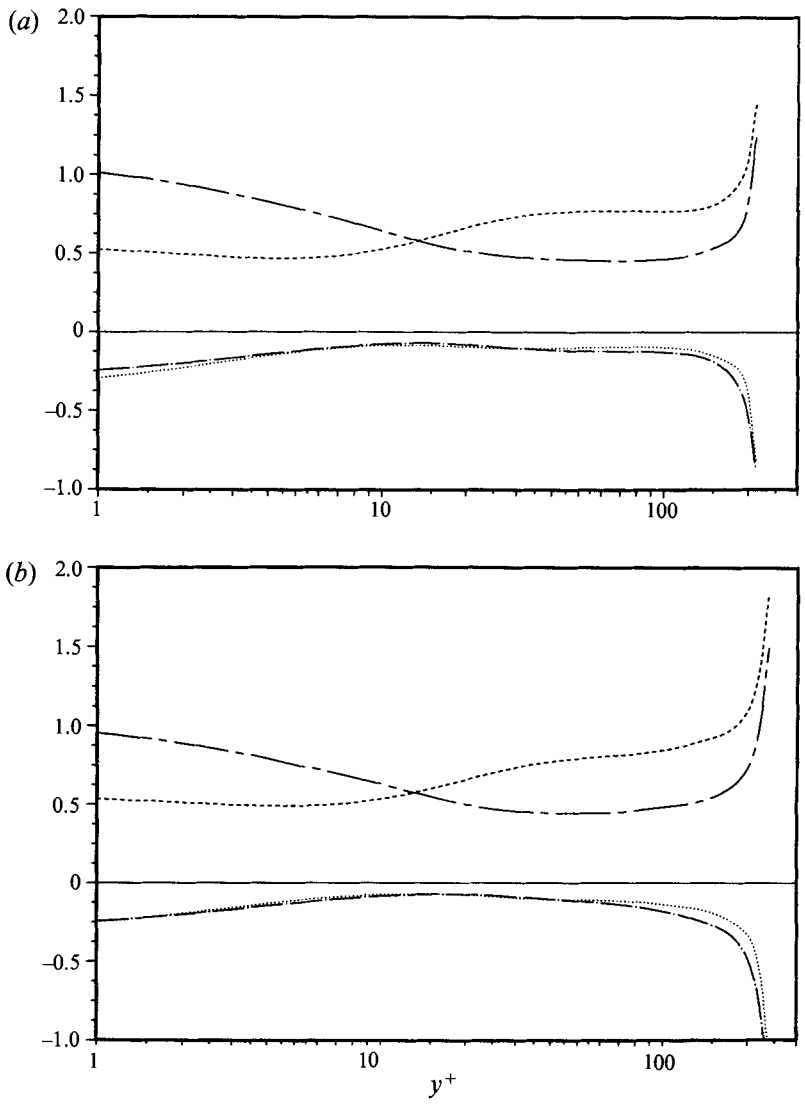

FIGURE 12. Reynolds shear stress for each quadrant normalized by the mean Reynolds shear stress: (*a*) $\gamma = 5$, (*b*) $\gamma = 11$: ·····, first; ——, second; — · —, third; ———, fourth quadrant.

contributions with curvature means that Reynolds shear stress events of any intensity contribute the same fraction of the total Reynolds shear stress in the transversely curved flows and in the plane channel. This is contrary to the measurements of Lueptow & Haritonidis (1987), who found that, in transversely curved flows, low-intensity Reynolds shear stress events accounted for a larger percentage of the total Reynolds shear stress than in the planar case.

The skewness factors of the velocity fluctuations, shown in figure 13, indicate that there is a strong effect of curvature on the streamwise and wall normal velocity fluctuations. As required by the reflective symmetry of the Navier–Stokes equations, the skewness of v_θ is zero everywhere. However, there are small deviations from zero in the computed statistics (≈ 0.1, not shown) which are due to the finite statistical sample.

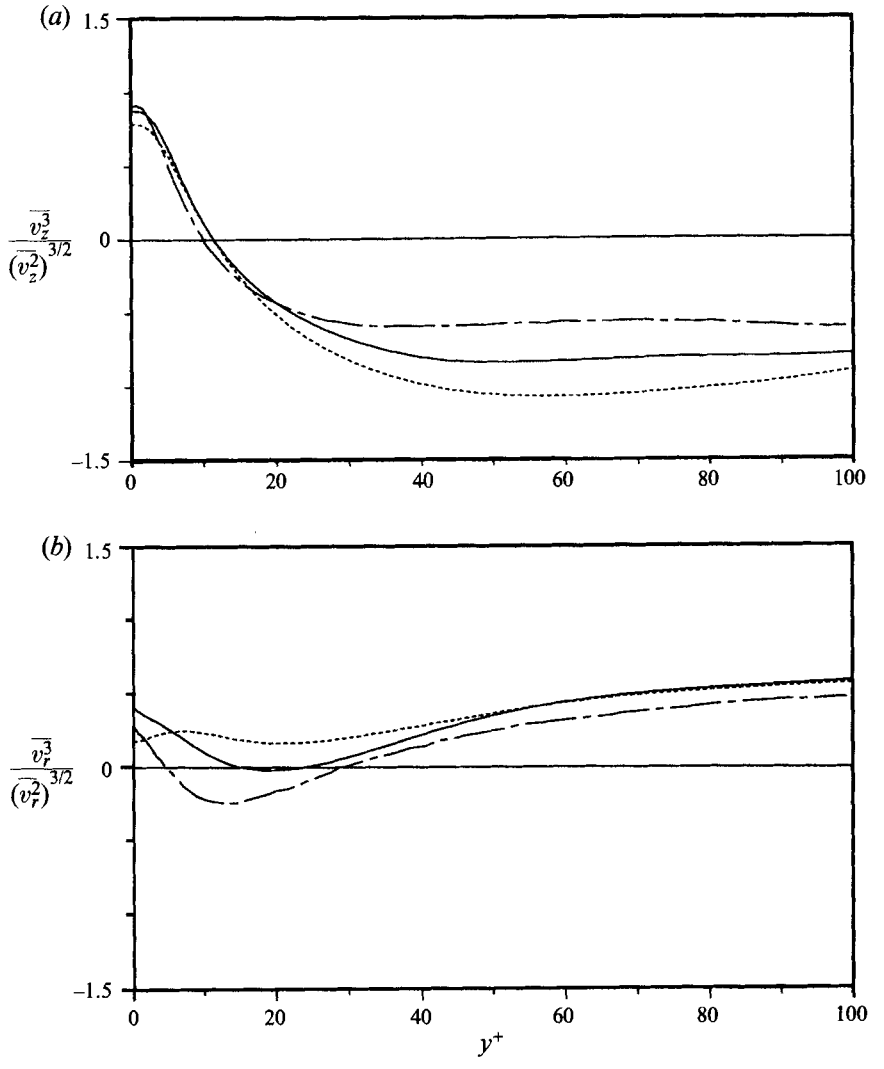

FIGURE 13. Skewness profiles of the velocity fluctuations: (*a*) $S(v_z)$ (streamwise), (*b*) $S(v_r)$ (wall-normal); ———, plane channel (Kim *et al.* 1987); cylinders with ——, $\gamma = 5$ and – – –, $\gamma = 11$.

Away from the wall ($y^+ > 40$), the skewness of v_r is positive and increases slightly with increasing curvature, as also observed by Luxton *et al.* (1984). In this region there are also strong negative streamwise velocity fluctuations, as denoted by the negative skewness of v_z, which decreases with increasing curvature.

Increasing the curvature does not significantly affect the skewness of the axial fluctuations (v_z) close to the wall ($y^+ < 20$). On the other hand, for $y^+ < 30$, there are significant differences in the skewness of the normal velocity fluctuations (v_r) between the three flows. While in the plane channel for $5 < y^+ < 30$ the skewness of v_r is negative, in the transversely curved flows the region of negative skewness diminishes and, for $\gamma = 11$, the skewness of v_r is positive throughout the layer. For $y^+ < 12$, where fourth-quadrant events dominate the Reynolds shear stress, the skewness of v_z is positive.

The flatness profiles of the velocity fluctuations are shown in figure 14. Near the wall

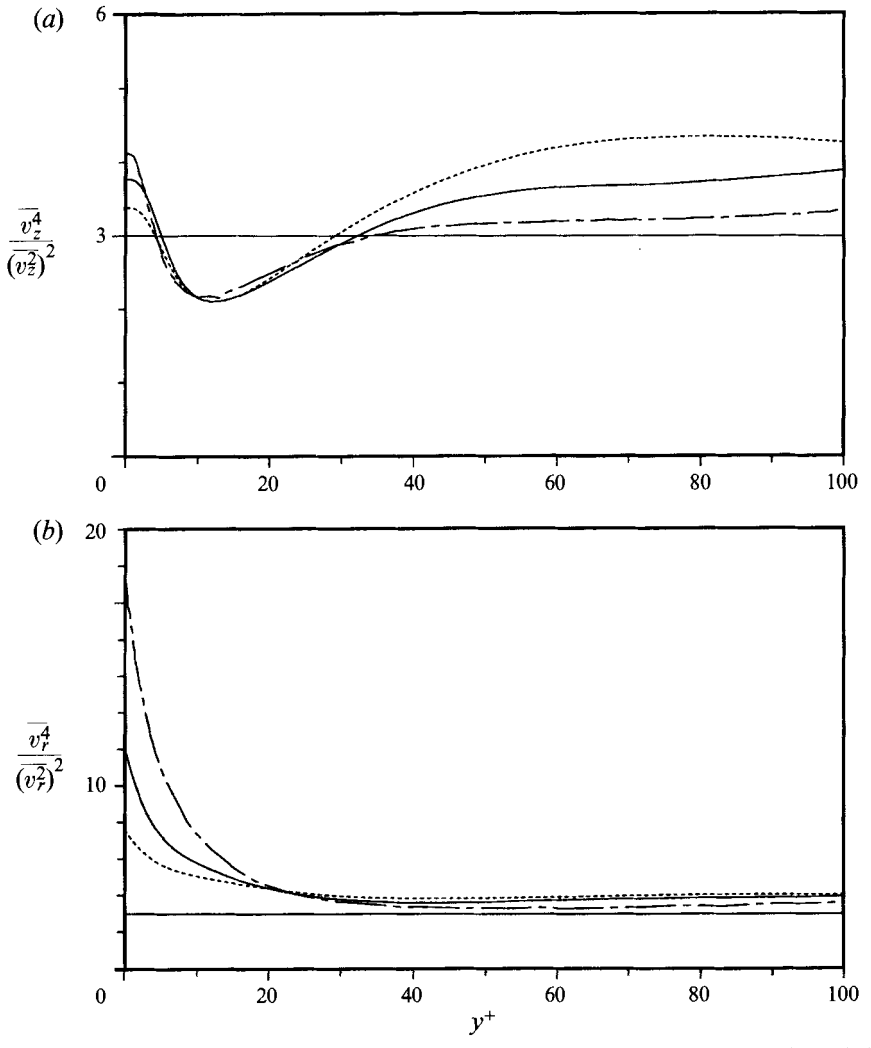

FIGURE 14. Flatness profiles of the velocity fluctuations: (*a*) $F(v_z)$ (streamwise), (*b*) $F(v_r)$ (wall-normal); ——, plane channel (Kim *et al.* 1987); cylinders with ——, $\gamma = 5$ and – – –, $\gamma = 11$.

($y^+ < 20$), the flatness of v_r decreases sharply with increasing curvature, indicating lower levels of intermittency. The flatness of v_z also decreases in the near-wall region ($y^+ < 5$). For $5 < y^+ < 30$ the flatness of v_z is not affected by the curvature and away from the wall ($y^+ > 30$) it increases with increasing curvature.

5. The vorticity

In cylindrical coordinates the vorticity components are given by

$$\left.\begin{aligned} \Omega_z &= \frac{V_\theta}{r} + \frac{\partial V_\theta}{\partial r} - \frac{1}{r}\frac{\partial V_r}{\partial \theta}, \\ \Omega_r &= \frac{1}{r}\frac{\partial V_z}{\partial \theta} - \frac{\partial V_\theta}{\partial z}, \quad \Omega_\theta = \frac{\partial V_r}{\partial z} - \frac{\partial V_z}{\partial r}. \end{aligned}\right\} \tag{14}$$

The vorticity intensities normalized by the mean wall shear stress, shown in figure 15,

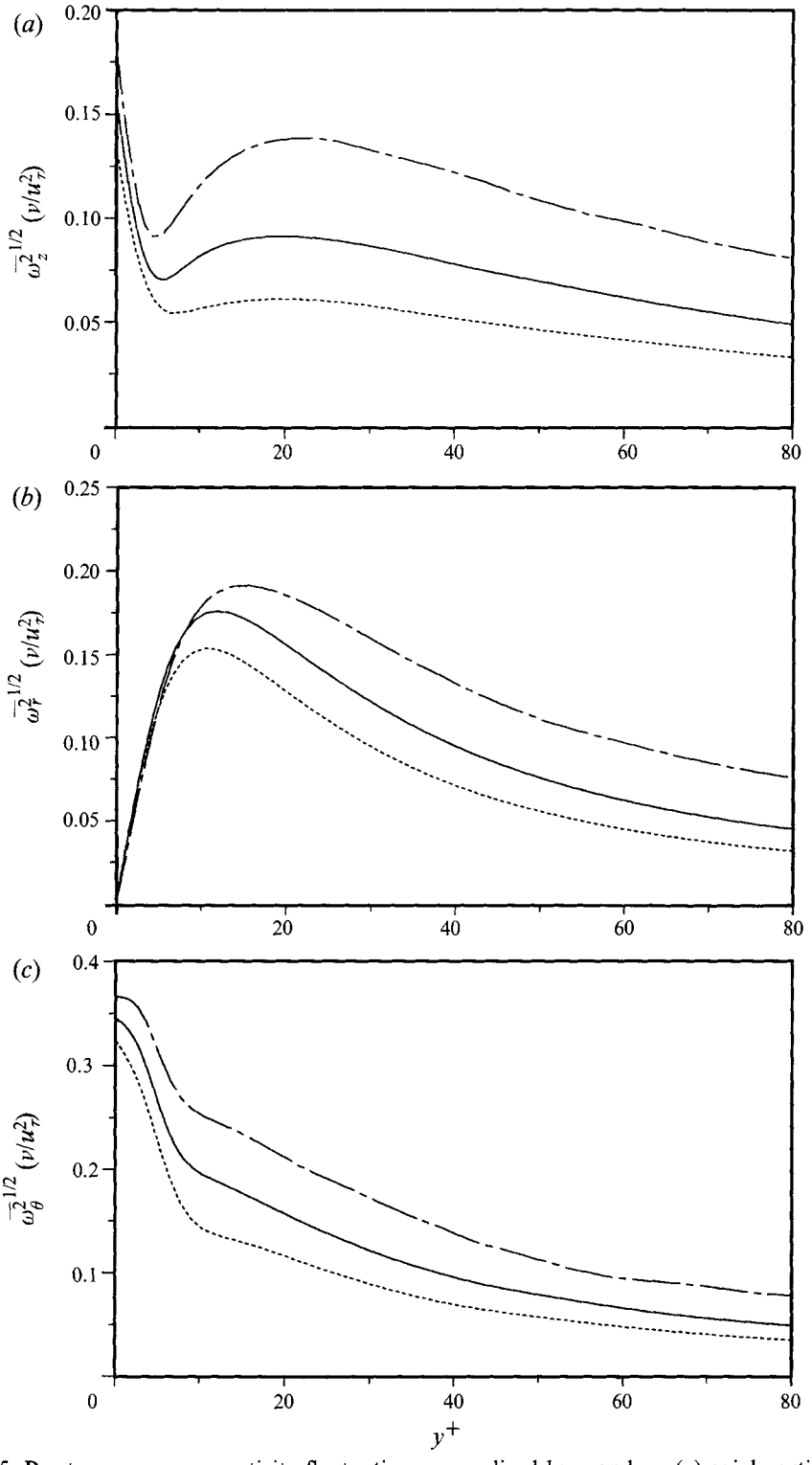

FIGURE 15. Root-mean-square vorticity fluctuations normalized by ν and u_τ: (*a*) axial vorticity, (*b*) normal vorticity, (*c*) azimuthal vorticity; ———, plane channel (Kim *et al.* 1987); cylinders with ——, $\gamma = 5$ and – – –, $\gamma = 11$.

γ	0	5	11
r_e^+	16.7	13.8	13.5
y_c^+	21.0	19.7	20.1
v_e^+	2.31	1.26	0.83
γ^+	0.139	0.092	0.061
Re_Γ	242.6	110.0	70.2

TABLE 6. Streamwise vortex parameters

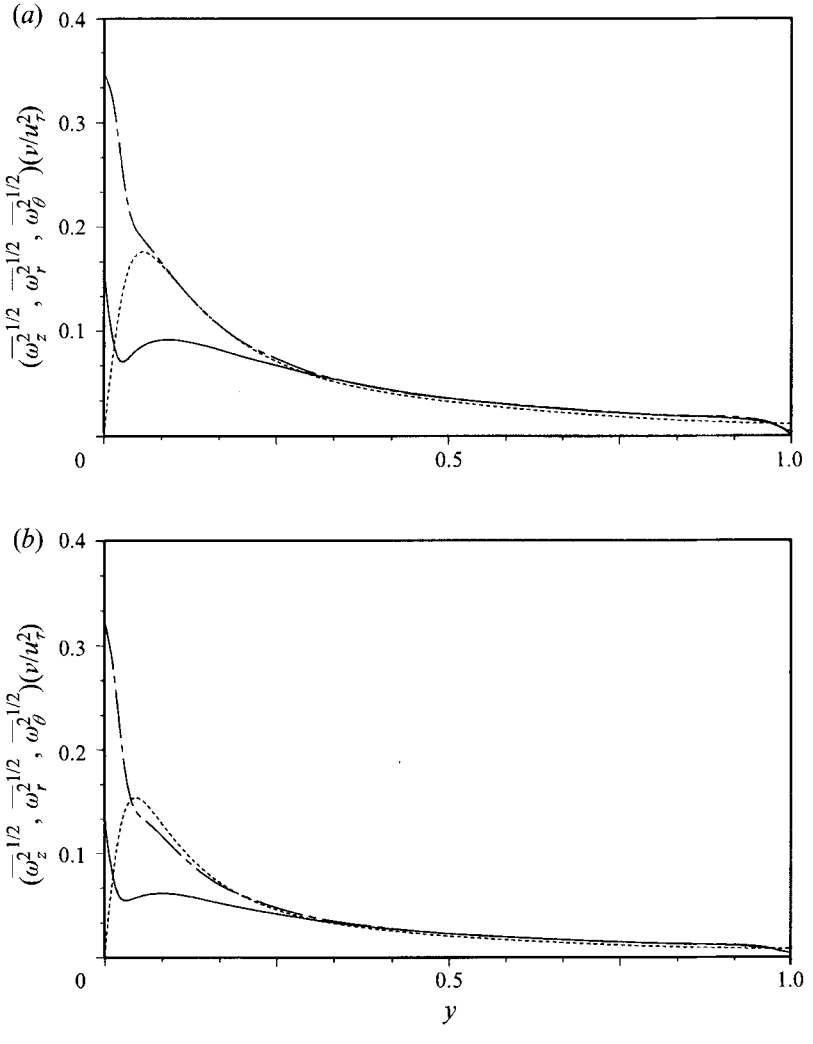

FIGURE 16. Root-mean-square vorticity fluctuations normalized by ν and u_τ in global coordinates for (*a*) $\gamma = 5$ and (*b*) $\gamma = 11$: ——, axial vorticity; — — —, azimuthal vorticity; – – –, normal vorticity.

decrease with increasing curvature. Unlike the velocity intensities, the vorticity intensities do not collapse in the outer part of the layer when scaled with the velocity scale $\tilde{u}$. As in the plane channel, the axial vorticity intensity exhibits a near-wall local minimum and local maximum. Kim *et al.* (1987) linked the locations and intensity of

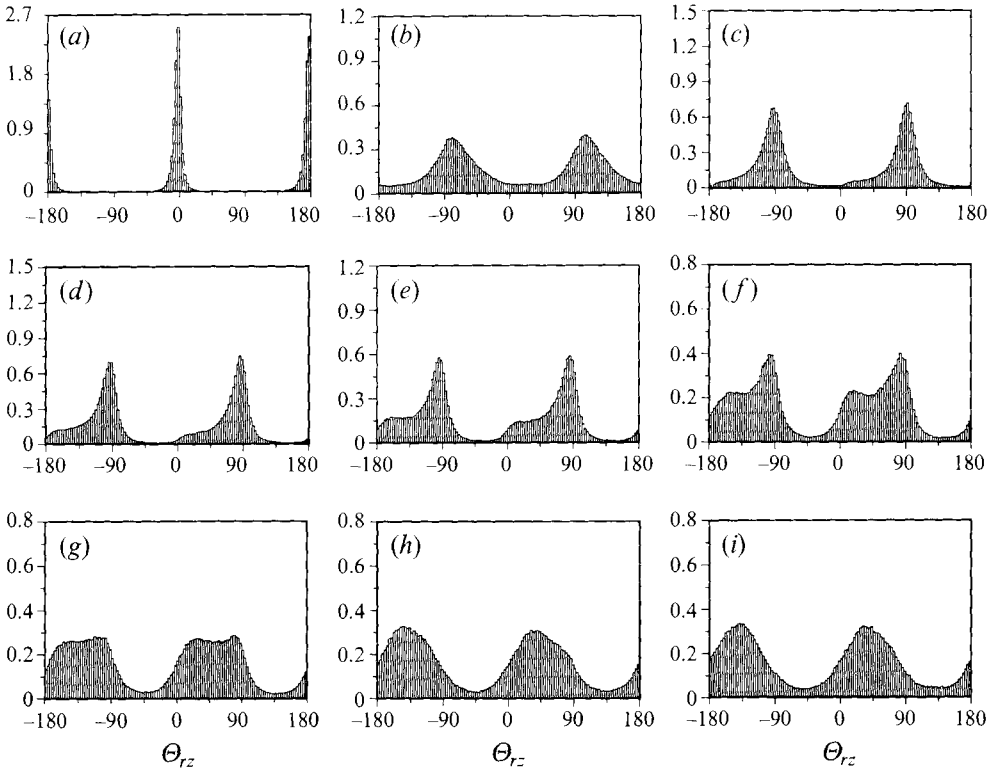

FIGURE 17. Distribution of the inclination angle, Θ_{rz}, of the projection of the vorticity vectors in (r,z)-planes for $\gamma = 5.0$; data weighted with the magnitude of the projected vorticity. (*a*) $y^+ = 0.66$; (*b*) $y^+ = 4.10$; (*c*) $y^+ = 8.02$; (*d*) $y^+ = 16.31$; (*e*) $y^+ = 25.38$; (*f*) $y^+ = 38.76$; (*g*) $y^+ = 51.85$; (*h*) $y^+ = 69.66$; (*i*) $y^+ = 96.25$.

these extrema to the average position and strength of the near-wall streamwise vortices. In their Rankine vortex model, the mean radius is estimated from the difference in the positions of the two extrema (y^+_{max}, y^+_{min}), $r^+_e = y^+_{max} - y^+_{min}$. The maximum value of the streamwise vorticity intensity is an estimate of the average strength (Γ) of the vortices, and the average tangential velocity at the edge of the vortices is given by $v^+_e = \Gamma^+ r^+_e$. The location of the maximum of the streamwise intensity (y^+_{max}) is an estimate of the mean position of the centres of the vortex cores.

These parameters and the vortex circulation Reynolds number,

$$Re_\Gamma = \frac{\Gamma}{\nu} = 2\pi v^+_e r^+_e, \tag{15}$$

are listed in table 6 for the two transversely curved flows as well as the plane channel of Kim *et al.* (1987). It is noteworthy that neither the core radius nor the position of the centre of these vortices changes appreciably with curvature, even though the strength of the vortices is greatly reduced.

There are other important curvature effects on the vorticity intensities. Near the wall ($y^+ < 7$), the normal vorticity intensity ($(\overline{\omega_r^2})^{1/2}$) is virtually unaffected by the curvature, while the other vorticity components decrease. In the outer part of the flow, as in the plane channel flow, the three components of the vorticity intensity are equal (figure 16). Further insight into the way in which the transverse curvature affects the near-wall

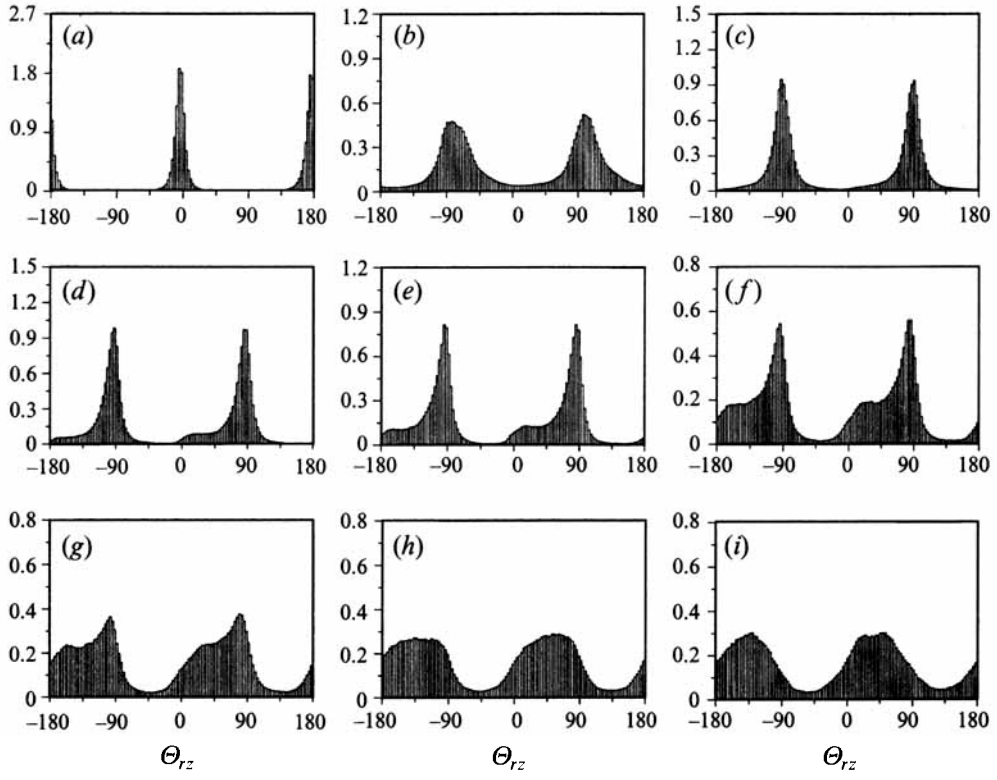

FIGURE 18. Distribution of the inclination angle, Θ_{rz}, of the projection of the vorticity vectors in (r,z)-planes for $\gamma = 11.0$; data weighted with the magnitude of the projected vorticity. (*a*) $y^+ = 0.72$; (*b*) $y^+ = 4.46$; (*c*) $y^+ = 8.74$; (*d*) $y^+ = 17.77$; (*e*) $y^+ = 27.66$; (*f*) $y^+ = 42.24$; (*g*) $y^+ = 56.52$; (*h*) $y^+ = 75.96$; (*i*) $y^+ = 104.90$.

axial and normal vorticity intensities can be gained by analysing the orientation of the vorticity field. Here, we follow the approach of Moin & Kim (1985). The inclination of the projection of the vorticity vector in (r,z)-planes is given by

$$\Theta_{rz} = \tan^{-1}\left(\frac{\omega_r}{\omega_z}\right). \tag{16}$$

The probability density functions (p.d.f.s) of Θ_{rz}, weighted by the magnitude of the projected vorticity vector (Moin & Kim 1985), $(\omega_r^2+\omega_z^2)/\langle\omega_r^2+\omega_z^2\rangle$, are shown in figure 17 for the $\gamma = 5$ flow and in figure 18 for the $\gamma = 11$ flow. In the expression above, $\langle\ \rangle$ indicates the mean of the quantity inside the brackets taken on the corresponding (z,θ) cylindrical surface. The following discussion refers to the weighted p.d.f.s, even though all the features described below are also evident in the unweighted p.d.f.s. The advantage of the weighting is that it enhances the contributions of the strong vorticity fluctuations.

Throughout the discussion of the orientation of the vorticity vector, the reader should bear in mind that the plane channel flow fields to which these results are compared were from the large eddy simulation of Moin & Kim (1985), which was performed for a Reynolds number of 13800 (based on the centreline velocity and channel half-width). At the closest point to the wall ($y^+ \approx 4$) investigated by Moin &

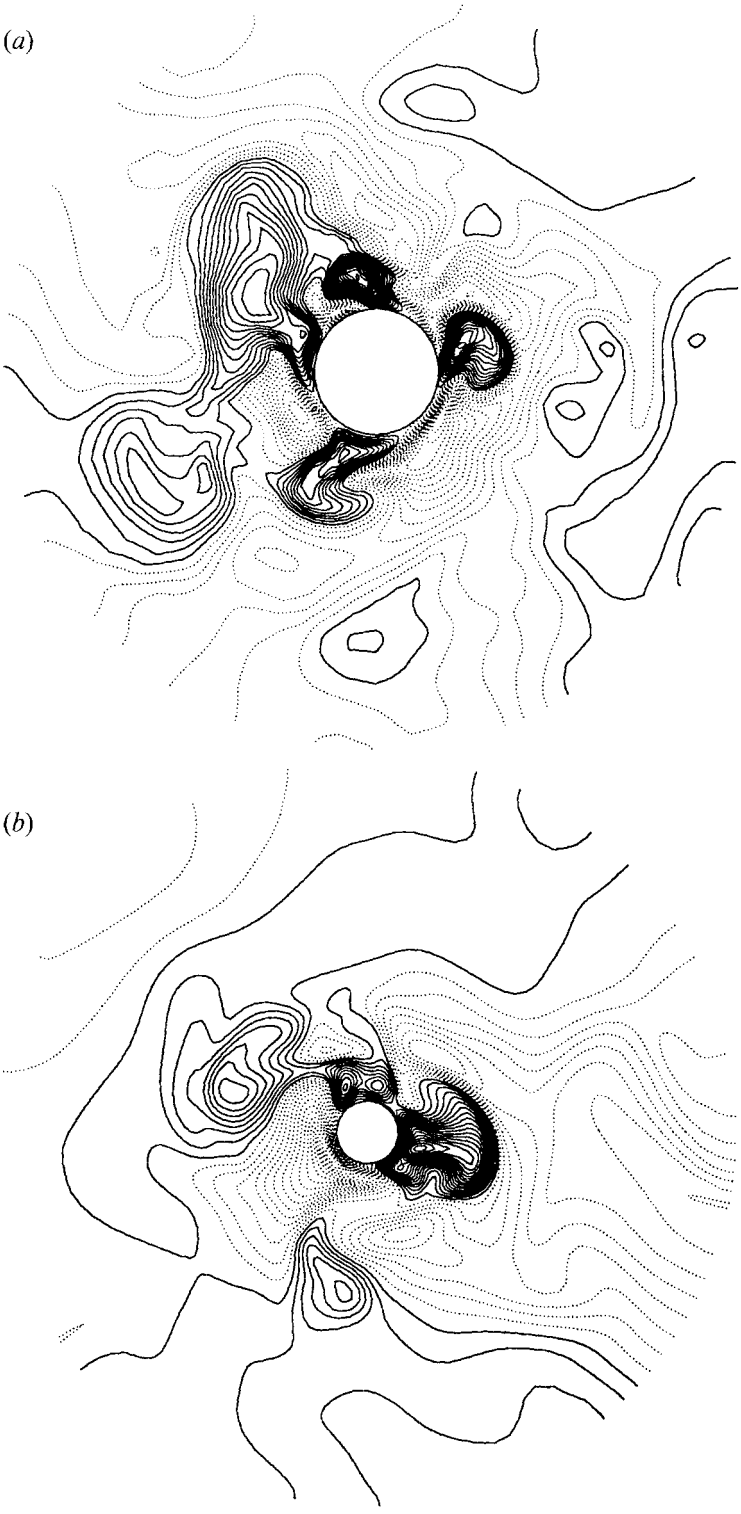

FIGURE 19. Contours of axial velocity fluctuations (v_z), normalized by u_τ, on a plane normal to the mean velocity: (*a*) $\gamma = 5$ with contour levels from $-5.2u_\tau$ to $3.55u_\tau$; (*b*) $\gamma = 11$ with contour levels from $-4.95u_\tau$ to $4.05u_\tau$. The contour increment is $0.25u_\tau$. Solid contours denote the low-speed fluctuations ($v_z < 0$) and the dotted contours denote the high-speed fluctuations ($v_z > 0$).

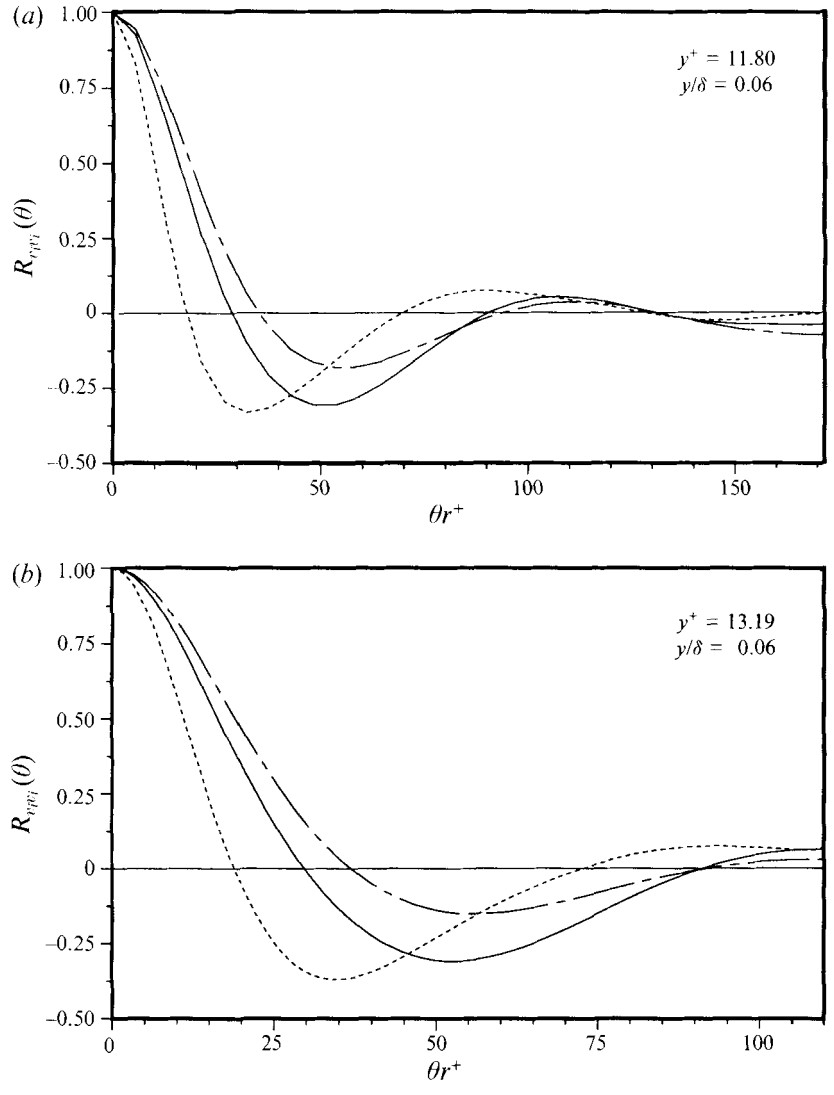

FIGURE 20. Azimuthal two-point correlations of the velocity fluctuations for (*a*) $\gamma = 5.0$ and for (*b*) $\gamma = 11$: ——, $R_{v_z v_z}$, – – –, $R_{v_r v_r}$, – – – –, $R_{v_\theta v_\theta}$.

Kim (1985), the distribution of Θ_{rz} is centred around 0° and $\pm 180°$ since the normal vorticity must go to zero at the wall owing to no-slip. In the transversely curved flows, this effect is not discernible in the histograms of Θ_{rz} for $y^+ > 2$. At $y^+ \approx 4$, both curved flows have distributions of Θ_{rz} that peak around $\pm 90°$. This distribution of Θ_{rz} persists up to $y^+ \approx 25$ in the $\gamma = 5$ flow and up to $y^+ \approx 40$ in the $\gamma = 11$ flow. Farther from the wall, the distributions gradually broaden, and by $y^+ \approx 52$ in the $\gamma = 5$ flow and $y^+ \approx 75$ in the $\gamma = 11$ the peak shifts to $-135°$ and 45° as was observed by Moin & Kim (1985).

Moin & Kim (1985) concluded that the main mechanism of vorticity stretching in the plane channel was stretching by the mean shear, which has its principal axis at 45° with the direction of the mean flow. When the normal and streamwise vorticity intensities are equal, the direction of the maximum vorticity in a shear flow is at 45° to the mean flow (Deissler 1969). As the curvature increases in the transversely curved flows, there

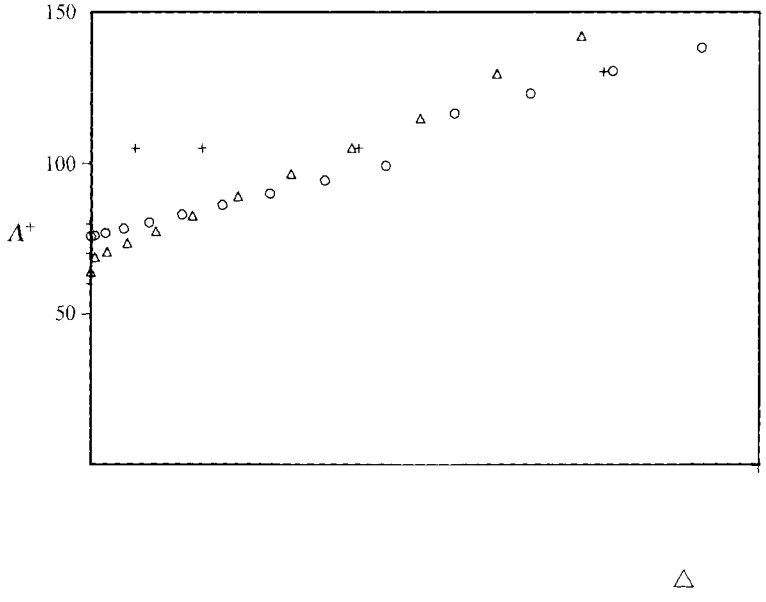

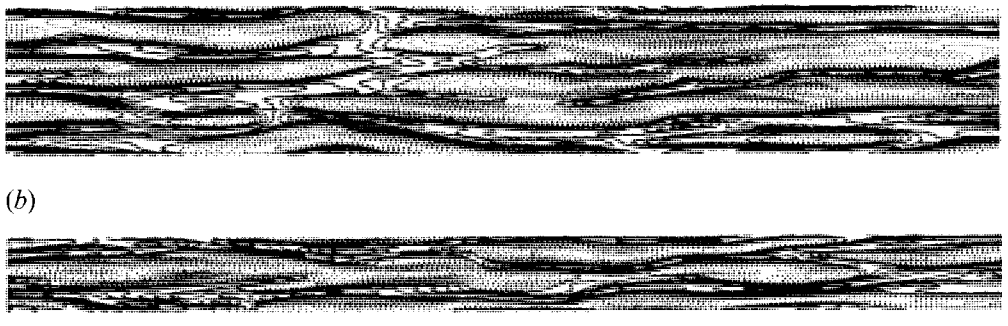

FIGURE 22. Contours of axial velocity fluctuations (v_z), normalized by u_τ and ν, on an unwrapped cylindrical surface at $y^+ \approx 5$: (*a*) $\gamma = 5$ with contour levels from $-2.2u_\tau$ to $5.55u_\tau$; (*b*) $\gamma = 11$ with contour levels from $-2.2u_\tau$ to $4.85u_\tau$. The axial length of the domain displayed is $3\pi\delta$ and the contour increment is $0.25u_\tau$. Solid contours denote the low-speed fluctuations ($v_z < 0$) and dotted contours denote the high-speed fluctuations ($v_z > 0$).

is an increasingly thicker layer around the cylinder, in which the vorticity has the $\pm 90°$ orientation. This suggests that, as the curvature increases, vortical structures inclined at 45° to the mean flow occur less frequently.

6. Instantaneous turbulent flow structures

Contours of the streamwise velocity fluctuations (v_z) on a (r, θ)-plane (normal to the mean flow) are shown in figure 19. In the smaller curvature case ($\gamma = 5$, see figure 19*a*), the circumference of the cylinder is about 270 wall units and in the snap-shot shown four low-speed streaks are observed around the cylinder. In the strongly curved case ($\gamma = 11$, see figure 19*b*), the perimeter of about 140 wall units apparently can only support two low-speed streaks. A better measure of the mean spacing between the low-speed streaks is given by the azimuthal (spanwise) velocity correlations shown in figure

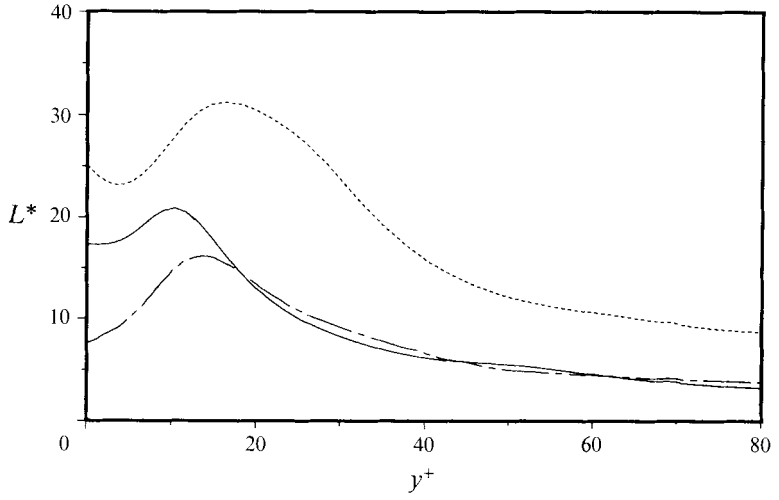

FIGURE 23. The lengthscale parameter $L^* = L^{(z)}/2L^{(\theta)}$ based on v_z: ———, plane channel (Lee *et al.* 1990); cylinders with ——, $\gamma = 5$ and – – –, $\gamma = 11$.

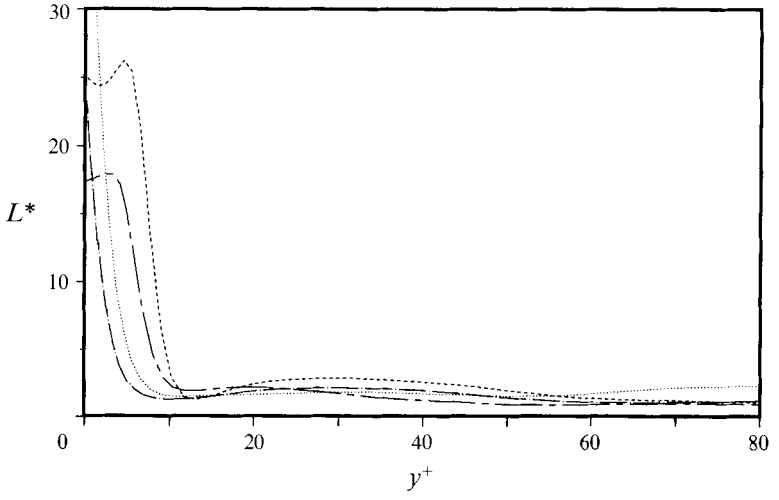

FIGURE 24. The lengthscale parameter: $L^* = L^{(z)}/2L^{(\theta)}$ based on ω_θ for cylinders with ———, $\gamma = 5$ and – – –, $\gamma = 11$; and based on ω_z for cylinders with —·—, $\gamma = 5$ and ·····, $\gamma = 11$.

20 (at $y^+ \approx 12$). When measured in viscous units, the mean streak spacing is about 100 in both flows. Note, however, that mean streak spacing Λ^+ is approximately proportional to r^+ (figure 21). Near the wall, this is a geometric effect owing to the variation of the local circumference with r.

The low-speed streaks can be seen in the contour plots of v_z on (z, θ) surfaces parallel to the cylinder at $y^+ \approx 5$ (figure 22). Note that the negative contours seem to be more elongated in the streamwise direction for the $\gamma = 11$ flow.

A measure of the anisotropy of the flow structures is the ratio of the streamwise to the spanwise lengthscales (Lee *et al.* 1990),

$$L^* = \frac{L^{(z)}}{2L^{(\theta)}}, \tag{17}$$

where $L^{(z)}$ and $L^{(\theta)}$ are the axial and azimuthal integral scales of the quantity of interest.

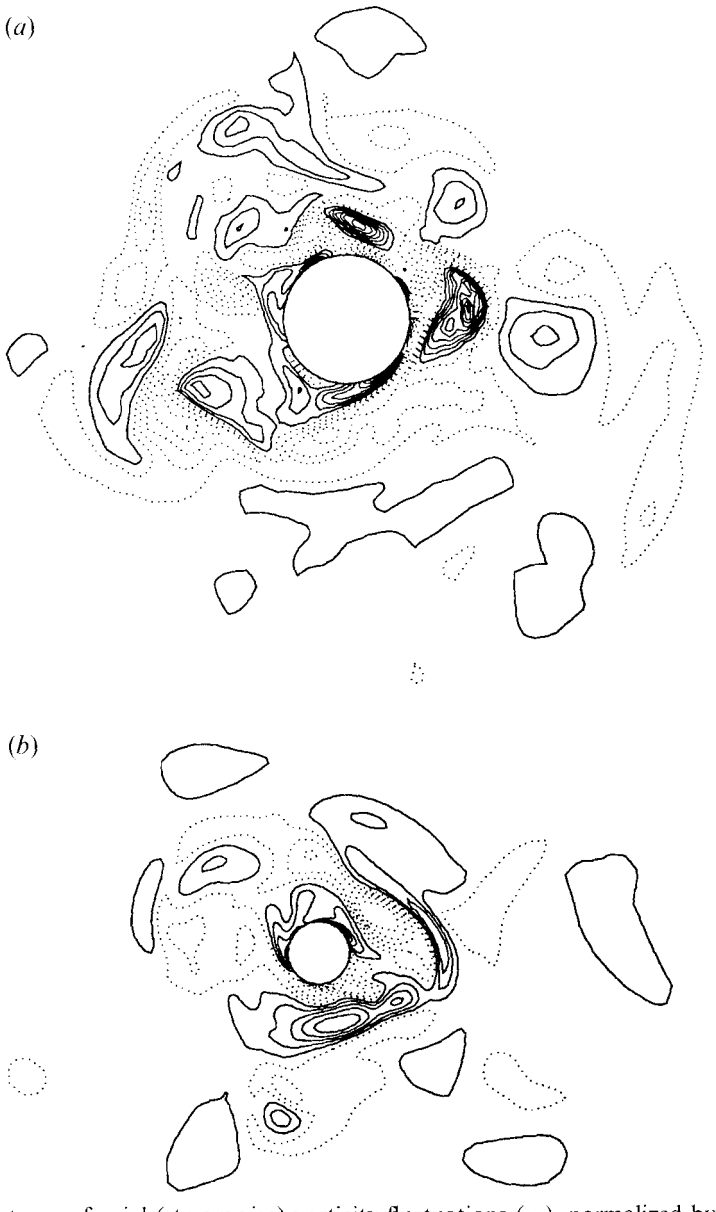

FIGURE 25. Contours of axial (streamwise) vorticity fluctuations (ω_z), normalized by u_τ and ν, on a plane normal to the mean velocity: (*a*) $\gamma = 5$ with contour levels from $-0.34u_\tau^2/\nu$ to $0.5u_\tau^2/\nu$; (*b*) $\gamma = 11$ with contour levels from $-0.3u_\tau^2/\nu$ to $0.38u_\tau^2/\nu$. The contour increment is $0.04u_\tau^2/\nu$. Solid contours denote negative vorticity ($\omega_z < 0$) and dotted contours denote positive vorticity ($\omega_z > 0$).

For example, when based on the axial (streamwise) velocity fluctuations, v_z, $L^{(z)}$ and $L^{(\theta)}$ are given by

$$L^{(z)}_{v_z}(y) = \int_0^{1/2L_z} R_{v_z v_z}(y, z)\,\mathrm{d}z, \quad L^{(\theta)}_{v_z}(y) = (a+y)\int_0^{\pi} R_{v_z v_z}(y, \theta)\,\mathrm{d}\theta, \tag{18}$$

respectively. L^* based on the streamwise velocity fluctuations (v_z), which characterize the low-speed streaks, was computed by Lee *et al.* (1990) for the plane channel; their

FIGURE 26. Contours of azimuthal vorticity fluctuations (ω_θ), normalized by u_τ and ν, on a (r,z)-plane through the axis of the cylinder. The axial length of the domain displayed is $3\pi\delta$: (*a*) $\gamma = 5$ with contour levels from $-0.74u_\tau^2/\nu$ to $0.56u_\tau^2/\nu$; (*b*) $\gamma = 11$ with contour levels from $-0.9u_\tau^2/\nu$ to $0.42u_\tau^2/\nu$. The contour increment is $0.04u_\tau^2/\nu$. Solid contours denote negative vorticity ($\omega_\theta < 0$) (aligned with the mean vorticity) and dotted contours denote positive vorticity ($\omega_\theta > 0$).

results are compared to the present simulations in figure 23. Close to the wall ($y^+ < 10$), L^* is significantly increased with increasing curvature. Since the spanwise lengthscale of the low-speed streaks in wall units is not greatly affected by curvature, their streamwise lengthscale must increase with γ. Away from the wall ($y^+ > 20$), L^* for the $\gamma = 5$ cylinder has essentially the same value as in the plane channel. In the larger curvature case ($\gamma = 11$) L^* away from the wall ($y^+ > 20$) is twice as large as its counterparts for the $\gamma = 5$ cylinder and the plane channel.

In addition to the low-speed streaks, near-wall flows are also characterized by near-wall vortical structures and internal shear layers. The lengthscale ratio defined in (18), computed for the axial (streamwise) and azimuthal (spanwise) vorticity fluctuations (ω_z and ω_θ), are shown in figure 24. For $y^+ > 10$, the lengthscale ratios for the two vorticity components are close to their isotropic value of unity. Near the wall ($y^+ < 10$), where the mean shear is largest, the lengthscale ratios of ω_θ and ω_z increase with increasing curvature. In particular, the higher near-wall L^* based on ω_z suggests that the near-wall streamwise vortices become longer as the curvature increases. Note also that both vorticity lengthscale ratios are only affected by curvature near the wall ($y^+ < 10$). The near-wall vortices are further illustrated in figure 25 which shows contour plots of the axial (streamwise) vorticity in (r,θ)-planes.

The near-wall shear layers that develop at the interface of the low- and high-speed flow regions are common in the two transversely curved flows as shown in figure 26 and have features similar to those of the plane channel. Figures 25 and 26 suggest that the higher curvature ($\gamma = 11$) flow is more quiescent in the outer region in agreement with the lower velocity correlation coefficient (figure 8). In figure 27 cross-sections of the internal shear layers by (r,θ)-planes show that the shear layers have large azimuthal (spanwise) lengthscales relative to the cylinder radius. As the curvature increases the ratio of the spanwise lengthscale of the shear layers to the cylinder radius increases. Cuts of these shear layers by (z,θ)-planes parallel to the cylinder (figure 28) at $y^+ \approx 15$ show a characteristic arrow shape that is more noticeable in the higher curvature ($\gamma = 11$) flow. These arrow shapes are the expected footprints of nearly planar inclined shear layers on the unwrapped cylindrical surfaces on which the vorticity contours are plotted in figure 28.

7. Summary and conclusions

The main objective of this part of the study was to investigate the characteristics of axial turbulent flows over long cylinders. For a sufficiently large ratio of the cylinder

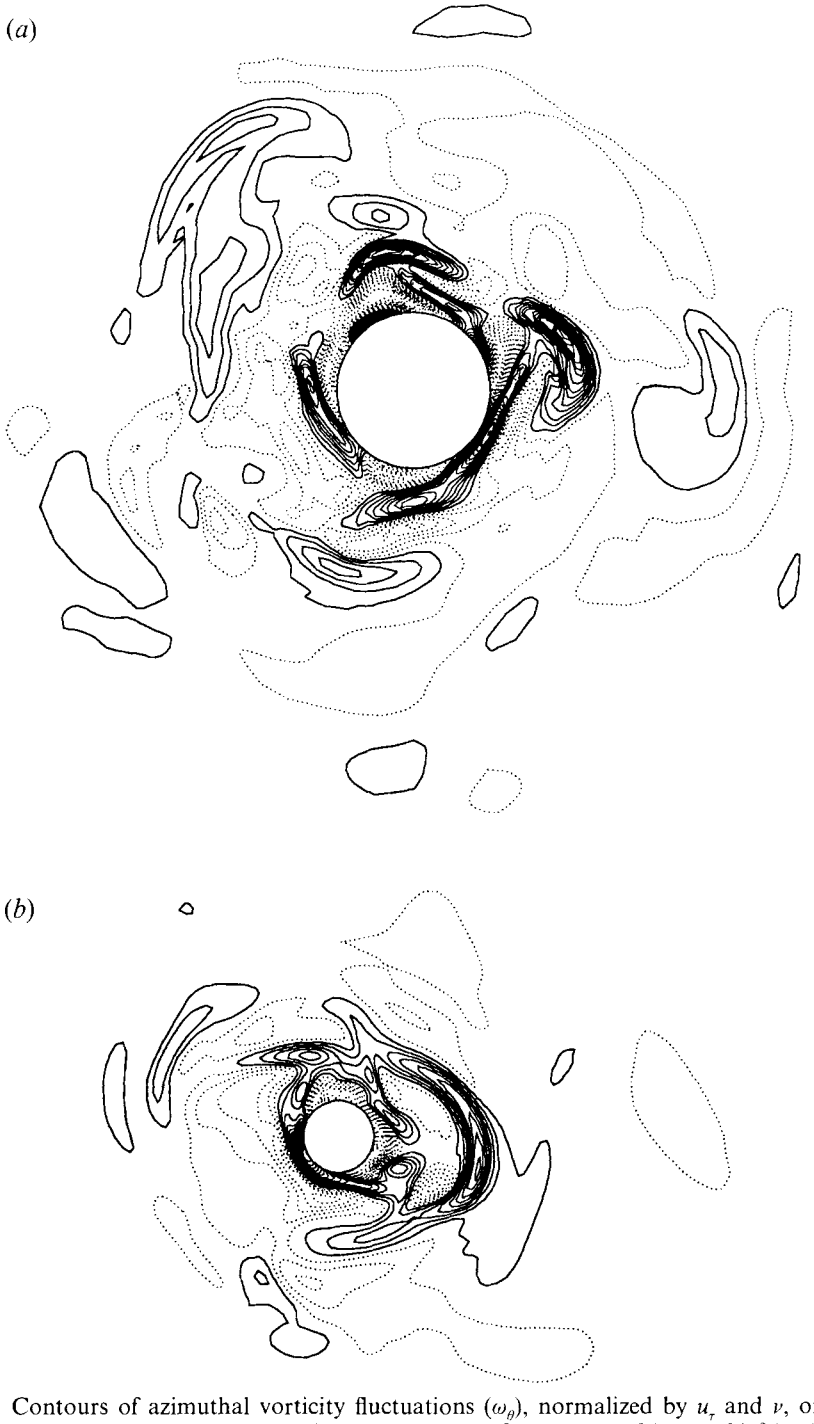

FIGURE 27. Contours of azimuthal vorticity fluctuations (ω_θ), normalized by u_τ and ν, on a plane normal to the mean velocity: (*a*) $\gamma = 5$ with contour levels from $-0.58u_\tau^2/\nu$ to $0.54u_\tau^2/\nu$; (*b*) $\gamma = 11$ with contour levels from $-0.66u_\tau^2/\nu$ to $0.5u_\tau^2/\nu$. The contour increment is $0.04u_\tau^2/\nu$. Solid contours denote negative vorticity ($\omega_\theta < 0$) (aligned with the mean vorticity) and dotted contours denote positive vorticity ($\omega_\theta > 0$).

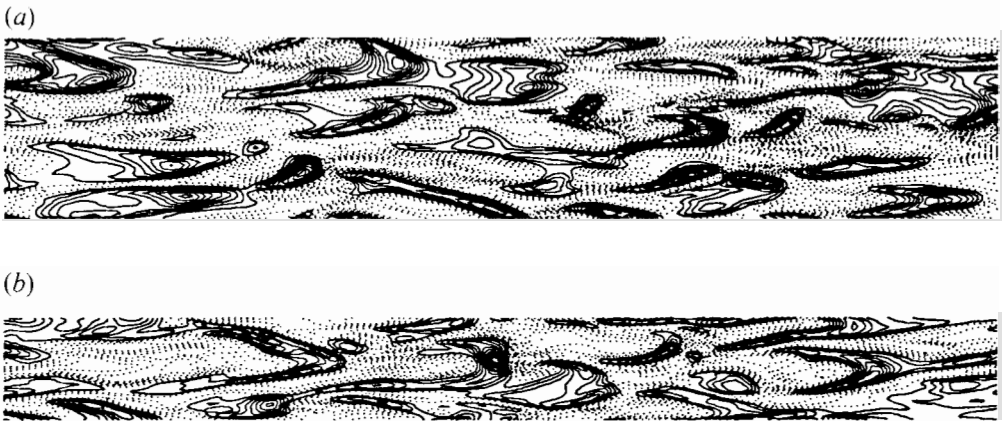

FIGURE 28. Contours of azimuthal vorticity fluctuations (ω_θ), normalized by u_τ and ν, on an unwrapped cylindrical surface at $y^+ \approx 15$. The axial length of the domain displayed is $3\pi\delta$: (*a*) $\gamma = 5$ with contour levels from $-0.58u_\tau^2/\nu$ to $0.32u_\tau^2/\nu$; (*b*) $\gamma = 11$ with contour levels from $-0.73u_\tau^2/\nu$ to $0.62u_\tau^2/\nu$. The contour increment is $0.05\ u_\tau^2/\nu$. Solid contours denote negative vorticity ($\omega_\theta < 0$) (aligned with the mean vorticity) and dotted contours denote positive vorticity ($\omega_\theta > 0$).

radius to the boundary-layer thickness (γ) curvature affects the outer part of the layer. If the inner flow is to be influenced by the curvature then the ratio of the cylinder radius to the viscous lengthscale au_τ/ν must also be small. Two simulations of transversely curved turbulent flows were performed; the curvature parameters were $\gamma = 5$ ($a^+ \approx 43$) and $\gamma = 11$ ($a^+ \approx 21$).

In agreement with experimental measurements, the skin friction coefficient (C_f) increases and the slope of the mean velocity profile in the logarithmic region decreases with increasing curvature. Turbulence intensities and the Reynolds shear stress (when scaled with wall variables) decrease with increasing curvature in the outer part of the flow, also in agreement with experimental data. However, unlike the experiments, in the computations these quantities also decrease with curvature near the wall. This difference is probably due to the large values of a^+ in most experiments. The distribution of the turbulent kinetic energy among the velocity components also changes with curvature, with the streamwise component taking an increasing fraction of the energy. This is a result of lower intercomponent energy transfer by the pressure strain correlations in the Reynolds stress budget equations.

A new velocity scale, which is a function of both the curvature parameter γ and the distance to the wall y has been obtained from the mean streamwise momentum equation. When normalized with this velocity scale some turbulence statistics of the plane channel and the transversely curved flows collapse in the outer part of the flow ($y^+ > 30$).

As the curvature increases, the correlation between the streamwise and wall normal velocity increases near the wall. In the higher curvature case ($\gamma = 11$) the correlation coefficient decreases in the outer layer indicating a tendency towards stabilization.

All vorticity intensities decrease with increasing curvature throughout the layer, with the exception of the normal vorticity intensity, which is not affected near the wall ($y^+ < 7$). The axial (streamwise) vorticity intensity profile suggests that, as the curvature increases, the near-wall streamwise vortices are weaker but have a radius similar to that of the plane channel. Their position relative to the wall is also not

affected by the curvature. As curvature increases, the vorticity vector near the wall tends to be increasingly oriented in the direction normal to the wall.

Another effect of the transverse curvature is the longer streamwise length of the low-speed streaks. The mean spanwise spacing of the low-speed streaks is less than 100 wall units very near the wall and increases to greater than 100 farther from the wall.

Near-wall internal shear layers are common in the two transversely curved flows computed. As the shear layers lift away from the surface of the cylinder they have large spanwise lengthscales relative to the cylinder radius.

We are indebted to Professors P. Bradshaw and S. Lele for many helpful discussions during the course of this study. We gratefully acknowledge the support of the Office of Naval Research, contract N00014-88-k-0145, and the Naval Underwater Systems Center, New London, CT 06320. NASA Ames Research Center provided the computer resources.

REFERENCES

AFZAL, N. & NARASIMHA, R. 1976 Axisymmetric turbulent boundary layer along a circular cylinder at constant pressure. *J. Fluid Mech.* **74**, 113–128.

AFZAL, N. & SINGH, P. 1976 Measurements in an axisymmetric turbulent boundary layer along a circular cylinder. *Aero. Q.* **27**, 217.

DEISSLER, R. G. 1969 Direction of maximum turbulent vorticity in a shear flow. *Phys. Fluids* **12**, 426–429.

DONNELLY, R. J. & SIMON, N. J. 1960 An empirical torque relation for supercritical flow between rotating cylinders. *J. Fluid Mech.* 7, 401.

GLAUERT, M. B. & LIGHTHILL, M. J. 1955 The axisymmetric boundary layer on a long thin cylinder. *Proc. R. Soc. Lond.* A **230**, 188.

GOTTLIEB, D. & ORSZAG, S. A. 1977 *Numerical Analysis of Spectral Methods: Theory and Applications.* CBMS-NSF Regional Conference Series in Applied Mathematics. SIAM 26, Philadelphia.

JIMENEZ, J. & MOIN, P. 1991 The minimal flow unit in near-wall turbulence. *J. Fluid Mech.* **225**, 213–240.

KIM, J., MOIN, P. & MOSER, R. D. 1987 Turbulence statistics in fully developed channel flow at low Reynolds number. *J. Fluid Mech.* **177**, 133–166.

KING, G. P., LI, Y., LEE, W., SWINNEY, H. L. & MARCUS, P. S. 1984 Wave speeds in wavy Taylor-vortex flow. *J. Fluid Mech.* **141**, 365–390.

KLEISER, L. & SCHUMANN, U. 1981 Treatment of incompressibility and boundary conditions in 3-D numerical spectral simulations of plane channel flow. *Proc. 3rd GAMM Conf. Numerical Methods in Fluid Mechanics* (ed. E. H. Hirschel), pp. 165–173. Vieweg, Braunschweig.

LEE, M. J., KIM, J. & MOIN, P. 1990 Structure of turbulence at high shear rate. *J. Fluid Mech.* **216**, 561–583.

LUEPTOW, M. R. 1988 Turbulent boundary layer on a cylinder in axial flow. *NUSC TR 8389.* Naval Underwater Systems Center, New London, CT 06320.

LUEPTOW, M. R. & HARITONIDIS, J. H. 1987 The structure of turbulent boundary layer on a cylinder in axial flow. *Phys. Fluids.* **30**, 2993–3005.

LUEPTOW, M. R., LEEHEY, P. & STELLINGER, T. 1985 The structure of turbulent boundary layer on a cylinder in axial flow. *Phys. Fluids.* **28**, 3495–3505.

LUXTON, R. E., BULL, M. K. & RAJAGOPALAN, S. 1984 The thick turbulent boundary layer on a long fine cylinder in axial flow. *Aero J.* **88**, 186.

MANSOUR, N. N., KIM, J. & MOIN, P. 1987 Reynolds-stress and dissipation-rate budgets in a turbulent channel flow. *J. Fluid Mech.* **194**, 15–44.

MOIN, P. & KIM, J. 1985 The structure of the vorticity field in turbulent channel flow. Part 1. Analysis of instantaneous fields and statistical correlations. *J. Fluid Mech.* **155**, 441–464.

MOSER, R. D. & MOIN, P. 1984 Direct numerical simulation of curved turbulent channel flow. *Rep. TF-20*. Department of Mechanical Engineering, Stanford University, Stanford CA 94305.

NEVES, J. C. & MOIN, P. 1994 Effects of convex transverse curvature on wall-bounded turbulence. Part 2. The pressure fluctuations. *J. Fluid Mech.* **272**, 383–406

NEVES, J. C., MOIN, P. & MOSER, R. D. 1992 Numerical study of axial turbulent flow over long cylinders. *Rep. TF-54*. Department of Mechanical Engineering, Stanford University, Stanford, CA 94305.

RAO, G. N. V. 1967 Law of the wall in a thick axisymmetric turbulent boundary layer. *Trans. ASME* E: *J. Appl. Mech.* **34**, 237.

RAO, G. N. V. & KESHAVAN, N. R. 1972 Axisymmetric turbulent boundary layer in zero pressure gradient flows. *Trans. ASME* E: *J. Appl. Mech.* **94**, 125.

REID, R. O. & WILSON, B. W. 1963 Boundary flow along a circular cylinder. *J. Hydraul. Div. Proc. ASCE* **89**, 21.

RICHMOND, R. L. 1957 Experimental investigation of thick axially symmetric boundary layers on cylinders at subsonic and hypersonic speeds. PhD thesis, California Institute Technology.

SEBAN, R. A. & BOND, R. 1951 Skin friction and heat transfer characteristics of a laminar boundary layer on a cylinder in axial incompressible flow. *J. Aero Sci.* **18**, 671–675.

SPALART, P. R. 1988 Direct simulation of a boundary layer up to $R_\theta = 1410$. *J. Fluid Mech.* **187**, 61–98.

WILLMARTH, W. W. & LU, S. S. 1972 Structure of the Reynolds stress near the wall. *J. Fluid Mech.* **55**, 55–92.

WILLMARTH, W. W., WINKEL, R. E., SHARMA, L. K. & BOGAR, T. J. 1976 Axially symmetric turbulent boundary layers on cylinders: Mean velocity profiles and wall pressure fluctuations. *J. Fluid Mech.* **76**, 35–64.

WILLMARTH, W. W. & YANG, C. S. 1970 Wall pressure fluctuations beneath turbulent boundary layer on a flat plate and a cylinder. *J. Fluid Mech.* **41**, 47–80.

YU, Y. S. 1959 Effects of transverse curvature on turbulent boundary layer characteristics. *J. Ship Res.* **2**, 33–51.